An evaluation of kilometer-scale ICON simulations of mixed-phase stratocumuli over the Southern Ocean during CAPRICORN

Veeramanikandan Ramadoss[1], Kevin Pfannkuch[1], Alain Protat[2], Yi HUANG[3], Steven Siems[4], and Anna Possner[1]

[1]Goethe University
[2]Australian Bureau of Meteorology
[3]The University of Melbourne
[4]MONASH UNIVERSITY

December 7, 2022

Abstract

This study investigates the representation of stratocumulus (Sc) clouds, cloud variability, and precipitation statistics over the Southern Ocean (SO) to understand the dominant ice processes within the Icosahedral Nonhydrostatic (ICON) model at the kilometer scale using real case simulations. The simulations are evaluated using the shipborne observations as open-cell stratocumuli were continuously observed during two days (26th -27th of March 2016), south of Tasmania. The radar retrievals are used to effectively analyze the forward-

simulated radar signatures from Passive and Active Microwave TRAnsfer (PAMTRA). We contrast cloud-precipitation statistics, and microphysical process rates between simulations performed with one-moment (1M) and two-moment (2M) microphysics schemes. We further analyze their sensitivity to primary and secondary ice-phase processes (Hallett–Mossop and collisional breakup). Both processes have previously been shown to improve the ice properties of simulated shallow mixed-phase clouds over the SO in other models. We find that only simulations with continuous formation, growth, and subsequent melting of graupel, and the effective riming of in-cloud rain by graupel, capture the observed cloud-precipitation vertical structure. In particular, the 2M microphysics scheme requires additional tuning for graupel processes in SO stratocumuli. Lowering the assumed graupel density and terminal velocity, in combination with secondary ice processes, enhances graupel formation in 2M microphysics ICON simulations. Overall, all simulations capture the observed intermittency of precipitation irrespective of the microphysics scheme used, and most of them sparsely distribute intense precipitation (>1mm h-1) events. Furthermore, the simulated clouds are too reflective as they are optically thick and/or have high cloud cover.

An evaluation of kilometer-scale ICON simulations of mixed-phase stratocumuli over the Southern Ocean during CAPRICORN

Veeramanikandan Ramadoss[1], Kevin Pfannkuch[1], Alain Protat[2], Yi Huang[3,4], Steven Siems[5]and Anna Possner[1]

[1]Institute for Atmospheric and Environmental Sciences, Goethe University, Frankfurt, Germany
[2]Australian Bureau of Meteorology, Melbourne, Victoria, Australia
[3]The University of Melbourne, School of Geography, Earth and Atmospheric Sciences, Melbourne, VIC, Australia
[4]Australian Research Council Centre of Excellence of Climate Extremes, Melbourne, Australia
[5]Monash University, Melbourne, VIC, Australia

Key Points:

- The continuous formation, in-cloud layer growth by riming, and sub-cloud layer melting of graupel are crucial to represent observed Southern Ocean stratocumulus cloud-precipitation structures during CAPRICORN.
- Boundary layer decoupling is reasonably captured in km-scale simulations when the positive bias in the prescribed ERA5 SST is removed.
- During CAPRICORN 2016, graupel melting is the predominant rain source in Southern Ocean stratocumuli as simulated in ICON.

Corresponding author: Veeramanikandan Ramadoss, `ramadoss@iau.uni-frankfurt.de`

Abstract

This study investigates the representation of stratocumulus (Sc) clouds, cloud variability, and precipitation statistics over the Southern Ocean (SO) to understand the dominant ice processes within the Icosahedral Nonhydrostatic (ICON) model at the kilometer scale using real case simulations. The simulations are evaluated using the shipborne observations as open-cell stratocumuli were continuously observed during two days (26$^{\text{th}}$-27$^{\text{th}}$ of March 2016), south of Tasmania. The radar retrievals are used to effectively analyze the forward-simulated radar signatures from Passive and Active Microwave TRAnsfer (PAMTRA). We contrast cloud-precipitation statistics, and microphysical process rates between simulations performed with one-moment (1M) and two-moment (2M) microphysics schemes. We further analyze their sensitivity to primary and secondary ice-phase processes (Hallett–Mossop and collisional breakup). Both processes have previously been shown to improve the ice properties of simulated shallow mixed-phase clouds over the SO in other models. We find that only simulations with continuous formation, growth, and subsequent melting of graupel, and the effective riming of in-cloud rain by graupel, capture the observed cloud-precipitation vertical structure. In particular, the 2M microphysics scheme requires additional tuning for graupel processes in SO stratocumuli. Lowering the assumed graupel density and terminal velocity, in combination with secondary ice processes, enhances graupel formation in 2M microphysics ICON simulations. Overall, all simulations capture the observed intermittency of precipitation irrespective of the microphysics scheme used, and most of them sparsely distribute intense precipitation ($>1\,\mathrm{mm\,h^{-1}}$) events. Furthermore, the simulated clouds are too reflective as they are optically thick and/or have high cloud cover.

Plain Language Summary

Stratocumulus (Sc) clouds cover a large portion of the Southern Ocean (SO), where they substantially cool the ocean surface. Our understanding of the complex physics of these clouds, which include both liquid and ice remains incomplete, and hence the representation of these clouds in global climate and weather models remains biased. In particular, their timing, frequency of occurrence, cloud phase and distribution, cloud cover, and precipitation characteristics are still associated with open research questions. This results in SO radiative biases and increased uncertainty for estimating climate sensitivity. We use the measurements from the Clouds, Aerosols, Precipitation, Radiation, and atmospherIc Composition Over the southeRn oceaN (CAPRICORN) voyage south of Tasmania, to evaluate the representation of broken cloud fields, the dominant ice processes, and the precipitation characteristics in the high-resolution numerical simulations. Our results suggest that, in addition to capturing the observed discrete cloud events, the graupel formation, its growth in the cloud layer, and subsequent melting in the sub-cloud layer are critical processes in accurately representing the SO broken Sc fields and precipitation characteristics during CAPRICORN. Additionally, compared to observations, the simulated clouds are too reflective.

1 Introduction

The Southern Ocean (SO) (45°S-65°S, 180°W-180°E) is one of the regions with the highest annually-averaged low cloud fraction of 60% (Muhlbauer et al., 2014). The low clouds, in particular, stratocumulus (Sc) clouds are capped by a strong temperature inversion of 10-20 K in just a few vertical meters at the top of the Sc topped boundary layer (Riehl et al., 1951; Caughey et al., 1982; Bosello et al., 2007). Cloud-top (CT) radiative cooling due to longwave emission is the most crucial mechanism that drives the convective instability to sustain Sc clouds, and further enhances the inversion at the CT. The supply of moisture from the ocean surface by latent heating, cooling from evaporation and sublimation in the sub-cloud layer (cold pool generation), the associated large-scale turbulent eddies, entrainment from the free tropospheric atmosphere at the CT, and precipitation are the processes interlinked with the mesoscale variability of Sc clouds (Bosello et al., 2007).

Precipitation and albedo strongly depend on the micro- and macrophysical properties, and the spatio-temporal distribution of hydrometeors within the Sc cloud field. A numerical weather or climate model must capture the aggregated effect of all these complex processes which occur at diverse spatial and temporal scales in its grid-scale tendencies and diagnostic variables.

A study by Bodas-Salcedo et al. (2012) with the atmosphere-only Met Office model reported that the low and mid-level clouds at the lee of the cold front of cyclones in the SO are responsible for the downwelling SW positive bias. The representation of Sc clouds largely differs in the 6$^{\text{th}}$ Coupled Model Intercomparison Project (CMIP6) compared to CMIP5 (Schuddeboom & McDonald, 2021). The SO Sc clouds were too few and too bright in CMIP5, whereas they occur more often in CMIP6, and are not brighter compared to Clouds and the Earth's Radiant Energy System (CERES) data. While a correct representation of cloud macrophysics alone is not a sufficient criterion, a better representation of cloud microphysics is essential for addressing the SW bias (Fiddes et al., 2022). The microphysics parameterization controls the shape, size, and concentration of liquid and ice hydrometeors in the SO Sc mixed-phase clouds (MPCs, and which strongly influence the cloud radiative effect.

Many models underestimate the presence of supercooled liquid water (SLW), since ice grows at the expense of liquid water in MPCs when the ambient vapor pressure is subsaturated and supersaturated with respect to liquid and ice respectively (termed as the Wegener-Bergeron-Findeisen process). The deficiency of the models in simulating supercooled liquid in SO MPCs can be compensated by slowing down the vapor deposition growth rate of ice crystals. This can be achieved by modifying the shape parameter of ice crystals. Although the focus is the SO, this has an impact on the liquid water content in either hemisphere (Varma et al., 2020). The ice formation process in mixed-phase Sc clouds is poorly understood (Fridlind et al., 2007), and the ice crystal number concentration (ICNC) is one of the largest uncertainties in these SO clouds. Heterogeneous nucleation requires ice nucleating particles (INPs) for droplet freezing where SLW prevails in metastable equilibrium. Nevertheless, the SO is a remote region with very low INP concentrations. For example, INP concentrations of 0.38 to $4.6\,\mathrm{m}^{-3}$ were observed at -20°C during March-April 2016 (McCluskey et al., 2018). The sparse INPs in SO limit droplet freezing and further the production of ice crystals, resulting in reduced precipitation and brighter clouds (Vergara-Temprado et al., 2018). However, a higher ICNC than INP concentration was observed during an earlier SO campaign. This was associated with the secondary ice production processes (Huang et al., 2017). The rime splintering process by Hallett and Mossop (1974), or HM, a predominant secondary ice production process in global climate models, is insufficient to account for the observed ICNC. The deficiency in the modeled ICNC in this remote atmosphere can be better described by HM in conjunction with collisional breakup processes (Sotiropoulou et al., 2020).

The objective of this paper is to investigate the significance of ice processes and the associated precipitation, and to understand the dominant microphysical processes in mixed-phase open-cell stratocumuli using numerical simulations. In this study, we evaluate the kilometer-scale ICON-NWP (Icosahedral Nonhydrostatic – Numerical Weather Prediction) simulations with the shipborne in-situ and remote sensing observations obtained during Clouds, Aerosols, Precipitation, Radiation, and atmospherIc Composition Over the southeRn oceaN (CAPRICORN) on 26$^{\text{th}}$-27$^{\text{th}}$ of March 2016, south of Tasmania. Among the numerous observations, a suite of instruments measured the cloud and precipitation characteristics, boundary layer structure, and surface energy fluxes during this first voyage of CAPRICORN (Mace & Protat, 2018a, 2018b). A set of convection-permitting simulations (referred to as "kilometer-scale") are performed in this study. The kilometer-scale simulations with active shallow-convection parameterization are used to address the following research questions in this study.

- How well do kilometer-scale ICON simulations capture the vertical structure of post-frontal mixed-phase cloud-precipitation in SO?
- How do different ice-phase processes impact precipitation formation in observed and simulated mesoscale cellular convective (MCC) clouds during CAPRICORN?
- Are these conclusions robust across different microphysics schemes of varied complexity available within ICON?

2 Observations, Simulations, and Analysis Methods

2.1 Observations

The CAPRICORN voyage I took place south of Tasmania from the 13th of March 2016 to the 15th of April 2016. During this time a consistent period of post-frontal open MCC clouds was observed between 26th and 27th of March 2016. The time period is characterized by a high-pressure system of 1030 hPa located south-west of Australia on the 26th of March 2016 (Figure 1a). A long cold front that stretches from 38°S-60°S, which is associated with the high-pressure system, passed the ship on 25th of March 2016 and Tasmania on 26th of March 2016. Open MCC clouds were observed for 36 hours at the lee of the cold front 6 hours later of its transit, followed by closed MCC clouds later on (Lang et al., 2021). Characterizing the clouds and precipitation properties and examining their occurrence statistics were part of the objective of the CAPRICORN field study using modern in-situ and remote sensing instruments aboard the R/V Investigator. A comprehensive overview of all instruments is provided in Mace and Protat (2018a, 2018b). Here, we only focus on measurements and retrievals relevant for this study.

The thermodynamic profiles of the atmosphere are obtained from radiosondes on 26th of March 2016 at 01:42:00 UTC and 06:24:00 UTC. The intensities of precipitation are observed from Ocean Rain and Ice-Phase Precipitation Measurement Network (OceanRAIN) disdrometer (Klepp, 2015). The downwelling SW radiation is measured from Precision Spectral Pyranometer (PSP) at the port and starboard sides of the R/V Investigator. The cloud-precipitation vertical structure is characterized by a 95-GHz single-polarization Bistatic Radar System for Atmospheric Studies (BASTA) Doppler cloud radar with a vertical resolution of 25 m and temporal resolution of 12 s (Delanoë et al., 2016). The cloud base phase (CBP) and the cloud base height (CBH) are derived from a 355 nm cloud-aerosol Leosphere RMAN-511 mini-Raman lidar with a vertical resolution of 15 m and temporal resolution of 35 s (Royer et al., 2014). The SST is measured from an in-situ instrument (which was the source of the sea surface temperature (SST) bias - see section 2.2.3) measures. The combined radar and lidar data (termed as the radar-lidar merged product) with a vertical resolution of 25 m and temporal resolution of 1-min is used to determine cloud phase. Temperature from the ERA-interim reanalysis is interpolated onto the pixels of the radar-lidar merged product. At sub-freezing temperatures, each pixel is classified as (a) SLW if only lidar signal is detected, (b) mixed-phase if lidar and radar signals are detected, and (c) mixed-phase or ice-phase if only a radar signal is present (Noh et al., 2019). The layer integrated lidar backscatter and lidar depolarization ratio (δ) are used (see section 2.3 for details) to determine CBH and CBP (Hu et al., 2009, 2010; Alexander & Protat, 2018; Mace & Protat, 2018a).

2.2 Simulations

2.2.1 Model Setup

Real case simulations are performed with ICON-NWP. The initial and hourly lateral boundary conditions are derived from the European Centre for Medium-Range Weather Forecasts fifth reanalysis (ERA5). The dynamical downscaling of ERA5 to the kilometer scale is achieved by a two-way nesting strategy (Figure 1b). Across three domains the horizontal resolution is roughly doubled each time from 4.9 km to 2.4 km to the highest

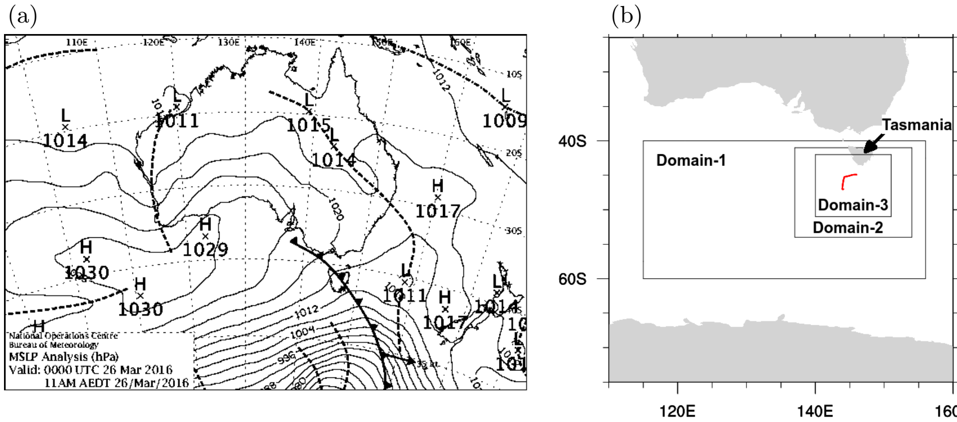

Figure 1: (a) Map of synoptic conditions south of Tasmania on 26$^{\text{th}}$ of March 2016 at 00 UTC. (b) ICON nested domains for simulation, where Domain-1 (outer domain) has 264948 cells with 4.9 km of horizontal resolution, Domain-2 has 304100 cells with 2.4 km of resolution, Domain-3 (highest resolution domain) has 556216 cells with 1.2 km of resolution, and the red line shows the ship track for two days (26$^{\text{th}}$-27$^{\text{th}}$ of March 2016).

resolution of 1.2 km. To minimize the numerical error in this study, the two-day (26$^{\text{th}}$ of March 2016 at 00:00:00 UTC to 28$^{\text{th}}$ of March 2016 at 00:00:00 UTC - case study period) simulation period was split into two 36 h time periods. The first 12 hours of each simulation are used as spinup. Furthermore, the last 12 hours of the first run (12 UTC of 25$^{\text{th}}$ of March until 00 UTC of 27$^{\text{th}}$ of March) overlap with the first 12 hours of the second run (12 UTC of 26$^{\text{th}}$ of March until 00 UTC of 28$^{\text{th}}$ of March). The model is run with 60 vertical layers and a model top height of 23 km. The layers within the boundary layer are stretched from 20 to 200 m in thickness. From Mellor and Yamada (1982), the turbulence scheme developed by Raschendorfer (2001) based on the prognostic turbulent kinetic energy (TKE) equation with 2$^{\text{nd}}$ order closure on level 2.5 is used. The rapid radiative transfer model (RRTM) developed by (Mlawer et al., 1997) is used for radiation. All convection is parameterized following the approach of Bechtold et al. (2008). In the kilometer-scale resolution domain (1.2 km), only shallow convection is parameterized. Horizontal cloud variability at the kilometer scale was best captured in simulations with parameterized shallow convection, which was thus kept turned on while all other convection parameterizations were turned off. All the runs with this setup are summarized in Table 1.

2.2.2 Microphysics Sensitivity Experiments

The sensitivity of the simulated cloud precipitation and cloud phase statistics are explored with respect to two different bulk microphysical schemes. The simpler, and computationally more efficient, one-moment (1M) scheme (Doms et al., 2011; Seifert, 2008) runs with fixed assumed number concentrations. Meanwhile a fully prognostic description of both, number and mass - and thus size-, is used in the two-moment (2M) scheme (Seifert & Beheng, 2006). The 1M control simulation (1M.90ND) is performed with a cloud droplet number concentration (CDNC) representative for SO austral conditions. This was determined as 90 cm^{-3} derived from the combined data of CAPRICORN I, II, and MARCUS (Measurements of Aerosols, Radiation, and Clouds over the Southern Ocean) for the austral summer months of November-April (Mace, Protat, et al., 2020). The sensitivity with respect to prescribed CDNC is investigated in an additional run with a lower prescribed CDNC of 20 cm^{-3} (1M.20ND), which is representative for austral autumn observations obtained during CAPRICORN I (Mace, Benson, & Hu, 2020) and austral winter aircraft observations (Ahn et al., 2017). In the 1M microphysics scheme, the ICNC is diagnosed using the temperature-dependent Cooper parameterization (Cooper, 1986), where heterogeneous ice nucleation occurs below a temperature threshold of -5°C.

Expt No.	Expt Name	Equation/Description
Bulk microphysics sensitivity experiments (Simulation period: 48 hours)		
1	1M.20ND	1M microphysics scheme and CDNC = 20 cm^{-3}
2	1M.90ND (control simulation)	1M microphysics scheme and CDNC = 90 cm^{-3}
3	2M.P	2M microphysics scheme and no secondary ice-phase processes
4	2M.HM	2M microphysics scheme with rime splintering secondary ice process
5	2M.HM.BR03	2M microphysics scheme with rime splintering and collisional breakup (rimed mass fraction is 0.3) secondary ice process
Microphysical process sensitivity experiments (Simulation period: 24 hours)		
1	2M.HM	Default: CCN = 400 cm^{-3}; power-law for $v_r = 95.5616 * exp(0.22 * log(x_r))$; Ice to snow minimum diameter threshold = 100 μm; low graupel density; low graupel velocity; graupel maximum diameter (= 2 mm); v_i = 27.7 * exp(0.21579 * log(x_i))
2	2M.P	Secondary ice production processes switched off
3	2M.HM.BR03	Collisional breakup with rimed mass fraction = 0.3
4	CCN10	CCN = 10 cm^{-3}
5	CCN1000	CCN = 1000 cm^{-3}
6	aukcc*0.5	Autoconversion cloud kernel coefficient is reduced by 50% (= 0.5*6E2)
7	aukcc*2	Autoconversion cloud kernel coefficient is doubled (= 2.0*6E2)
8	ice_vel_coef	v_i = 317 * exp(0.363 * log(x_i))
9	rain_atlas	v_r = 9.292 - (9.623 * exp(-622.2 * a_geo * exp(b_geo * log(x_r))))
10	agg_50	Aggregated ice to snow minimum diameter threshold = 50 μm
11	agg_200	Aggregated ice to snow minimum diameter threshold = 200 μm
12	gr_d_m	$d_g = 0.3456 * {x_g}^{0.3571}$ (Medium lump graupel density)
13	gr_d_h	$d_g = 0.3456 * {x_g}^{0.3704}$ (High lump graupel density)
14	gr_v_h	$v_g = 9.4465 * {x_g}^{0.12}$ (High lump graupel velocity)
15	gr_max_dia	Graupel maximum diameter increased to 5 mm

Table 1: Bulk microphysics sensitivity experiments for the entire simulation period (26th of March 2016 at 00:00:00 UTC to 28th of March 2016 at 00:00:00 UTC) and microphysical process sensitivity experiments with 2M microphysics scheme (simulated on 27th of March 2016). v, terminal velocity of hydrometeors in $m\,s^{-1}$; d, diameter of hydrometeors in m; x, mass of hydrometeors in kg; v_{sed_i} is maximum sedimentation velocity of ice; CCN, cloud condensation nuclei; CDNC, cloud droplet number concentration; a_geo and b_geo constants in rain hydrometeor mass - fall speed relation; subscripts r, i and g represent rain, ice and graupel respectively.

To better understand the significance of ice processes in SO mixed-phase Sc clouds, sensitivity experiments were carried out with the 2M scheme since it has control over CCN and INP specifications. The cloud-precipitation vertical structure and the precipitation statistics as the result of cloud ice processes are studied using sensitivity experiments: 2M.P, 2M.HM, and 2M.HM.BR03 described in Table 1. The collisional breakup parameterization developed by Phillips, Yano, and Khain (2017); Phillips, Yano, Formenton, et al. (2017) based on the principle of ejected fragments as a function of the initial collisional kinetic energy of solid hydrometeors is implemented for ice, snow and graupel in ICON. The parameterization of prognostic CDNC is adapted from Segal and Khain (2006) and the prognostic ICNC from Seifert and Beheng (2006). The activation scheme for CDNC is computed for a prescribed lognormal aerosol size distribution with a mean number concentration of $400\,\mathrm{cm}^3$ and a mean radius of $0.04\,\mu m$ (see supporting information S2). Immersion freezing for sea spray aerosols is parameterized by McCluskey et al. (2018) and dust aerosol by Demott et al. (2015); McCluskey et al. (2019). These adjustments to the default heterogeneous freezing parameterization Seifert and Beheng (2006) were performed to better capture the remote aerosol environment of the SO relevant for INP nucleation. A fictitious increase of the potential INPs at low temperatures was avoided by relaxing INP concentrations exponentially with height over 4 km. Immersion freezing rates are limited to temperatures at or below -5°C. A small perturbed physical parameter ensemble is performed for 2M simulations for a range of parameters related to the simulated graupel budget (G_budget) in SO stratocumuli. In addition to dynamics, the formation and depletion of graupel is based on the sensitivity of the interlinked microphysical processes. The impact of various factors that can influence these microphysical processes and further the G_budget is analyzed (microphysical process sensitivity experiments in Table 1).

2.2.3 SST Bias Correction

During CAPRICORN, the instruments for measuring SST were at the ship deck from 22$^{\mathrm{th}}$-26$^{\mathrm{th}}$ of March 2016. This biased the assimilation of SST in ERA-Interim, ERA5, and MERRA-2 products by upto 6°C (Lang et al., 2021). This artificially increases the sea–air temperature differences, which may have an impact on surface cold pools, boundary layer decoupling, and the average inversion height. Hence, we corrected the bias by limiting the maximum SST to 12°C in the entire simulation domain (Figure S1a). We thus ran the simulations essentially with prescribed SST of 12°C along the track. This fix improved the overall match between observed and simulated SST and surface fluxes shown in Fig S1, but fails to capture the 1-2°C increase in SST after 36 hours which coincides with the transition of sampling open-cell cloud structures to solid cloud decks towards the end of the 48 hours period (Figure 2a).

2.3 Analysis Methods

Minimum thresholds are applied in the simulations for all hydrometeor categories. These are specified as $0.01\,\mathrm{g\,m^{-3}}$ for cloud liquid, $0.0001\,\mathrm{g\,m^{-3}}$ for cloud ice, and $0.00001\,\mathrm{g\,m^{-3}}$ for rain, snow, graupel, and hail. The simulated cloud-top height (CTH), cloud-top phase (CTP), CBH and CBP are identified based on these thresholds. Two-dimensional field statistics are computed in a clipped zone (147° $\geq$ lon $\geq$ 143°; -44° $\geq$ lat $\geq$ -48°) enclosing the ship track. The retrieved CTH along the ship track has been derived from the ground-based BASTA radar reflectivity profile. Lidar backscatter is very sensitive to the water droplet population and attenuates completely within a few tens of meters of the cloud. It is thus a reliable measure for identifying the CBH. We cannot use the minimum height of the first backscatter signal of the lidar to determine the cloud base (CB), as this metric may be biased low by precipitation. Instead, the CBH is calculated as the altitude at which the maximum vertical gradient of backscatter occurs. The phase partitioning at the CBH is based on the threshold values for δ (ratio of perpendicular to parallel backscatter intensities with respect to the transmitter polarization axis). The depolarization ratio is very small for cloud water and smaller raindrops since the parallel backscatter predominates. Mace and Protat (2018a) suggest $\delta \leq 0.02$ for liquid-dominant layers and $\delta \geq 0.03$ for ice-dominant layers. We assumed a mixed-phase category in the in-between range. Since lidar backscatter is influenced by densely populated hydrometeors in the resolution volume, we are more likely to miss the presence of ice at CB. Hence we include an additional criterion one level below the identified CB to correct the CBP as ice-phase if $\delta \geq 0.03$ and the temperature is less than 3°C. The CB precipitation is calculated as the average precipitation in the lowest one-third of the cloud depth as defined by Wood (2005).

We analyze the microphysical processes with 1M and 2M microphysics schemes to examine the shortcomings in representing the cloud-precipitation vertical structure. The microphysical processes are normalized by the total water vapor loss to the ice-phase (Equation 1) to understand their relative importance, as shown in Equation 2.

$$\begin{aligned} WVL^*(n,k,i) =& {X^*}_{nuc}(n,k,i) + {X^*}_{I\_dep}(n,k,i) + {X^*}_{S\_dep}(n,k,i) \\ &+ {X^*}_{G\_dep}(n,k,i) + {X^*}_{H\_dep}(n,k,i) \end{aligned} \tag{1}$$

$$\overline{X}(n,k,i) = \frac{\sum\limits_{n,k,i}^{t,4km,nclip} X^*(n,k,i)\; V(n,k,i)}{\sum\limits_{n,k,i}^{t,4km,nclip} WVL^*(n,k,i)\; V(n,k,i)} \tag{2}$$

Here, V is the cell volume (m^3); WVL* is the total water vapor loss to the ice-phase (kg m^{-3} s^{-1}); X* is the rate of the mass density for a given microphysical process (kg m^{-3} s^{-1}); ${X^*}_{\mathrm{nuc}}$, ${X^*}_{\mathrm{idep}}$, ${X^*}_{\mathrm{sdep}}$, ${X^*}_{\mathrm{gdep}}$, ${X^*}_{\mathrm{hdep}}$ are the rate of mass density of ice nucleation, ice deposition, snow deposition, graupel deposition and hail deposition (kg m^{-3} s^{-1}) respectively; $\overline{X}$(i,j,k) is calculated for a time period t (index n), up to 4 km altitude (index k) and the spatial extent (index i) is clipped around the ship track (nclip: $147° \geq lon \geq 143°$; $-44° \geq lat \geq -48°$).

Furthermore, the forward simulated ICON output from the Passive and Active Microwave TRAnsfer (PAMTRA) model (Mech et al., 2020) is evaluated against the BASTA radar retrievals. For evaluating the simulation with CAPRICORN, the mean of the simulated data within 2 km at each coordinate along the ship track is used. The supporting information S1 provides a basic setup of PAMTRA for 1M and 2M simulations.

3 Results

Cloud and precipitation characteristics during CAPRICORN between the 26$^{\mathrm{th}}$ and 27$^{\mathrm{th}}$ of March 2016 have been studied in great detail in Lang et al. (2021). They hypothesized that ice processes could play a significant role in the SO open-cell precipitation during this period. In this section, we use the retrieved cloud properties and precipitation characteristics from the observations to evaluate the skill of kilometer-scale ICON simulations (control simulation). Collected soundings (Figures S2a and S2b) are compared to the simulated soundings in the post-frontal environment of the control simulation (1M.90Nd). Note, that the second sounding is the thermodynamic profile obtained during the open-cell period. While the overall profiles are well captured, the inversion height is underestimated by at least 200 m during the open-cell period (Figure S2b). The transition layer that separates the two observed cloud layers is located at 1.2 km (0.9 km), and 1.7 km (1.8 km) in the first and second observed (simulated) sounding respectively. Although the simulated CTH is underestimated in the second profile, the simulated mean CTH along the ship track is slightly overestimated at 2.2 km as compared to the observed 1.8 km.

3.1 Evaluation of Cloud-Precipitation Vertical Structure and Statistics

The vertically pointing single-polarization Doppler radar reflectivity is used to evaluate the vertical cloud and precipitation structures. Figure 2a shows that intermittent radar reflectivities occur throughout the two days characterizing sporadic precipitation events.

The increase in reflectivity across the melting layer is caused by the higher reflectivity of liquid hydrometeors than previously frozen hydrometeors (i.e. cloud ice, snow and graupel). The melting of solid hydrometeors produces liquid precipitation of reduced size, which is characterized by a higher terminal fall velocity than ice particles due to an increase in density. This is clearly visible in the more negative Doppler velocities below the melting layer (Figure S3a). Furthermore, this decrease in Doppler velocity across the melting layer is well captured by the simulations. However, the mean Doppler velocity of melted rain seems biased low (falling faster) in 1M.90ND. Furthermore, the presence of ice above the freezing line is further supported by the merged radar-lidar product (Figure 2c). Most streaks (also termed as cloud events) above the melting level are classified as mixed-phase, or consist of adjacent patches of ice and SLW.

To understand the formation and evolution of precipitation in the cloud and the cloud-precipitation vertical structure, we generate (Figure 2a) a contoured frequency by altitude diagram (CFAD) from the BASTA radar reflectivity retrieval. The CFAD is normalized by the total samples in every reflectivity bin. The numbers at the top of the CFAD denote the number of samples within a reflectivity bin (summed along all altitudes) normalised by the maximum number of samples (summed across all altitudes) in one reflectivity bin found across all reflectivity bins. The CFAD aggregates the cloud-precipitation data of the same reflectivity-height bins across multiple timestamps. Thus a physical relationship between bins across heights may no longer be given. However, a statistical analysis of all observed vertical reflectivity profiles (Figures S4a) which exclude “single data” points (“single data” here refers to the presence of just one single, isolated data point within the column) shows that, overall 14.7% of all streaks exceed 0 dBz in the lowest 0.4 km (white box in Figure S4b). Furthermore nearly all points within this region originated from higher layers and follow a trajectory of increasing reflectivity with decreasing height (negative inclination). Similarly 20.8% of all streaks reach low reflectivities of -25 dBZ below 1.2 km. This time a positive inclination can be observed backtracking these points where reflectivities increase with altitude. Thus, in this case, the CFAD provides a mean representation of the aggregated vertical evolution of precipitation.

We hypothesize that the negative inclination (0 to 20 dBZ; <1.2 km) in Figure 2e refers to the melting of solid hydrometeors, enhanced melting of graupel, growth of raindrops by selfcollection (collision-coalescence), and larger ice hydrometeors coated with the layer of liquid water. However, the melting of small ice crystals doesn’t cause significant changes in radar reflectivity and thus cannot contribute to the negative inclination in the CFAD. Processes involving the growth of graupel particles (riming, deposition, and collisional growth) are unlikely to contribute to the downward slope as virtually no solid surface precipitation was observed during CAPRICORN.

Between the positive and negative inclined slopes, the in-cloud layer hydrometeors are visible along a zero-slope bridge structure (-20 to 10 dBZ between 1.2 and 1.6 km). The continuous cloud-precipitation events that pass through the bins within -35 dBZ to -25 dBZ, and 0.4 km to 1.2 km, account for 17.3% of the total timestamps (Figures S4e,f). Furthermore, most of these events begin above 1.2 km and disappear before reaching 0.4 km. This is in good agreement with the physical hypothesis presented for the positive inclination, which is likely driven by the partial evaporation or sublimation of sedimenting rain or ice. Fall streaks disappearing between 1.2 km and 0.4 km then correspond to precipitation events which fully sublimated or evaporated before reaching the surface.

This arc structure which characterizes the dominant evolution of precipitation observed during CAPRICORN is well pronounced in the control simulation (Figure 2f). However, the link (from -5 to 0 dBZ; 1.2 to 1.6 km altitude) between the bridge (here, simulated bridge refers the bright band from -25 to 0 dBZ; 1.6 to 2 km altitude) and the downward slope band is poorly represented. This bias is likely caused by the absence of a melting scheme within PAMTRA and the low vertical resolution of the model output. From the negative inclination of the arc (reflectivity band between 0 and 20 dBZ), the cloud-precipitation streaks from the bridge firmly reduce to 24%, 11% and 9% below 1.2 km towards near-surface, whereas 25%, 24% and 26% were observed during CAPRICORN. The decreasing percentage is either related to a steady decline in raindrop size due to evaporation if the downward change in reflectivity of the streaks is negative, or an increase in raindrop size due to collision-coalescence if the downward change in reflectivity is positive. Meanwhile, percentage increases are associated with an abrupt loss in raindrop size as the reflectivity streaks pass through the multiple reflectivity bins inside the height bins less than 0.4 km. This may result in larger raindrops in the control simulation as their evaporation is more effective at altitudes below 0.4 km in CAPRICORN. To better understand the origin of the bridge structure, the contribution of each hydrometeor species was analyzed individually. This was done to get a sense of the relative importance between the individual hydrometeor species. However, one cannot expect the individual contributions listed in Table S1 to be additive. We find that graupel hydrometeors alone contribute 66% to the total bridge reflectivity structure in the control simulation. Thus in ICON, precipitation statistics are largely influenced by the in-cloud formation and sub-cloud layer evolution of graupel.

Here, we compare the simulated statistics and variability of precipitation between observations and simulations across a single track observed from the ship over a two-day period. Thus, it is unlikely that these single track measurements capture the entire variability of the low cloud-precipitation system. To account for that, we generate a small ensemble of theoretical tracks in the simulations to compare against the observations. In addition to the ship route, 10 additional tracks are constructed with a 0.2 degree offset (Figure S5). This yields a total of 11 tracks across which the simulated statistics from point measurements are compared with the observations. The normalized CFAD considering the full track ensemble (Figure S6) for the control simulation qualitatively agrees with its same simulation (Figure 2f) just one versus 11 tracks. An average decline in mean bridge reflectivity over all tracks of 10.2% was simulated. This indicates that the single-track observations over this time period are sufficiently long to characterize the variability of spatio-temporal intermittent vertical precipitation structures.

Figure 2d shows that the simulated cloud phase (see section 2.3 for the definition) along the ship track qualitatively agrees with the phase distinction of the merged radar-lidar product (Figure 2c). Furthermore, the simulated MPCs are enriched with graupel. It is evident that all of the graupel particles (hatching in Figure 2d) melt near the melting level. In general, radar reflectivity increases towards the ocean surface by collision-coalescence that efficiently occurs on larger raindrops. The larger raindrops are more likely to occur either due to the high ambient relative humidity at low levels that reduces the homogenization of the rain drop size spectrum through evaporation. Additionally, weaker updrafts in comparison with the raindrop fall velocity (weaker convection) can contribute to this effect as the vertical segregation by rain drop sedimentation speed is amplified. Most of the simulated surface precipitation timestamps in the ship track exhibit this phenomenon along the reflectivity streaks. Additionally, the mean Doppler velocity (MDV) also shows the growth in raindrop size driven by collision-coalescence (Figure S3b). For example, the precipitation rate of 5.6 $\mathrm{mm\,h^{-1}}$ immediately after the 24$^{\mathrm{th}}$ hour (Figure 3b) has an increase in reflectivity of >20 dBZ (Figure 2b) near the ocean surface. Similarly, the MDV decreases to -3.5 $\mathrm{m\,s^{-1}}$ below the melting level but slightly increases to -3.3 $\mathrm{m\,s^{-1}}$ below 0.4 km. This may be due to the partial evaporation of the raindrops near the ocean surface. The subcloud evaporative cooling from precipitation reduces the near-surface air temperature and increases the relative humidity. The decrease in near-surface air temperature is connected with the emergence of a surface cold pool, which is a significant criterion for boundary layer decoupling. Further, this increases the surface SHF and decreases the surface LHF. Increased SHF and decreased LHF are driven by the increase in the difference between the near-surface air temperature and SST for the former and increased RH for the latter. These processes were well observed during CAPRICORN (Lang et al., 2021), and across many timestamps in the control simulation (Figure 3a).

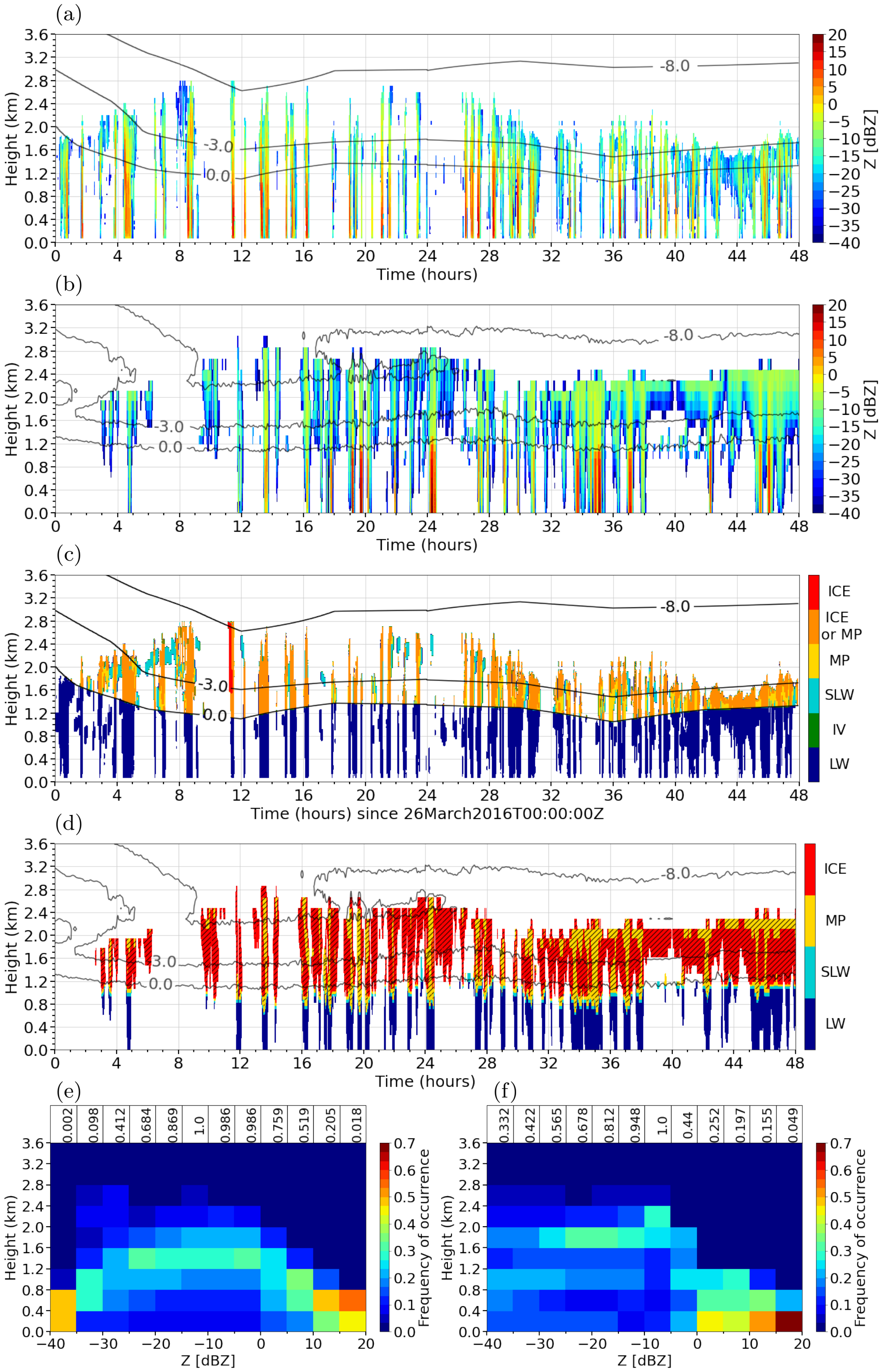

Figure 2: Time-height cross-section with 1-min temporal resolution of (a) BASTA radar reflectivity, (b) simulated radar reflectivity, (c) observed radar-lidar merged cloud-precipitation phase and (d) simulated cloud-precipitation phase. Isotherms in °C (black lines). Normalized contoured frequency by altitude diagrams (CFAD) with 1-min resolution for the case study period of (e) observed radar reflectivity and (f) simulated reflectivity. Simulated data corresponds to control simulation. Case study period: 26$^{\text{th}}$ of March 2016 at 00:00:00 UTC to 28$^{\text{th}}$ of March 2016 at 00:00:00 UTC. IV, ice virga; MP, mixed-phase; LW, warm liquid water.

Among the total cloud-precipitation occurrence fraction of 71.1% along the ship track for 1M.90ND, 3.6% occurs within the first 6 hours (succeeded by closed to open cells transition or advection) and 24.8% occurs in the final 12 hours of the simulation period. Similarly, among the total cloud-precipitation occurrence fraction of 52.4% observed during CAPRICORN, 6.4% occurs within the first 6 hours and 19.5% occurs in the final 12 hours of the simulation period. This negative bias in the initial period and the positive bias in the final period for the cloud-precipitation occurrence fraction may be the result of the SST bias correction. A positively biased SST can cause excessive deepening of the boundary layer by overestimating the entrainment of free tropospheric dry air, which can cause the underestimation of the low-cloud fraction (Bretherton & Wyant, 1997; Sandu & Stevens, 2011; Lang et al., 2021). The initialized SST is positively biased during the first 6 hours of the simulation period and negatively biased during the final 12 hours (Figure S1a), explaining why the simulated occurrence fraction or cloud development was lower for the former and higher for the latter.

Figure 3b shows that low precipitation rates are observed during CAPRICORN and 1M.90ND until the onset of open-cell MCC (open-cell period: 06 to 42 hours). Furthermore, the total accumulated precipitation is realistic at the end of the two days (Figure 3c). Precipitation hardly occurs in the control simulation until 19 hours, whereas frequent precipitation events are observed during this period in the open-cell region. The mean (95$^{\text{th}}$ percentile) precipitation rate of CAPRICORN and the control simulation are 0.046 mm h^{-1} (0.05 mm h^{-1}) and 0.051 mm h^{-1} (0.13 mm h^{-1}) respectively. In addition, the occurrence of only few of these events can drastically alter the accumulated precipitation as seen after 20 and 24 hours. Although the timing of 1M.90ND precipitation rates doesn't agree well with the observations along the ship track, the interquartile range of quasi-ensemble accumulated precipitation shows an outstanding agreement with the observations (Figure 6b). The control simulation is skewed to the right (Figure S7), which shows that the stronger precipitation events ($>$1 mm h^{-1}) are sparsely distributed with a mean frequency of occurrence of 3.17 as compared to CAPRICORN with 3.67. Furthermore, the variability of the accumulated precipitation increases considerably in the the southeast of the CAPRICORN track, while it differs modestly for most of the tracks in the northwest region (Figure S7 and Table S2).

The time series of surface precipitation is well aligned with the radar reflectivity profiles in both observation and 1M.90ND. Thus we can combine both measurements to learn more about near-surface precipitation characteristics. By correlating the radar reflectivities at 75 m altitude (where ground BASTA radar first detected the signal) and the observed surface precipitation, the minimum reflectivity associated with at least 1 mm h^{-1} of surface precipitation is 1 dBZ. However, 52.6% of surface precipitation rates lower than 1 mm h^{-1} are associated with reflectivities larger than 1 dBZ. Using the PAMTRA reflectivities for 1M.90ND and the surface precipitation rates, 1 mm h^{-1} are associated with a considerably larger minimum reflectivity of 10.8 dBZ. However, only 38.2% of lower precipitation rates are associated with higher reflectivities. Similarly, for precipitation rates of at least 1 mm h^{-1} to occur, a maximum criteria of -1.96 m s^{-1} (-2.86 m s^{-1}) MDV is identified for CAPRICORN (1M.90ND). Yet, 71.4% (24.5%) of lower precipitation rates fall below this criteria. As a result, the minimum reflectivity (maximum MDV) criteria during the occurrence of surface precipitation above 1 mm h^{-1} with respect to minimum reflectivity (maximum MDV) is positively (negatively) biased for the control simulation. Furthermore, the number of events having precipitation rates below 1 mm h^{-1} with respect to the minimum reflectivity and maximum MDV is negatively biased for the control simulation (Figure S3b). Since reflectivity is proportional to the sixth power of the size of hydrometeors of similar phase and MDV decreases with an increase in the size of hydrometeors, this reveals that the control simulation generates larger near-surface raindrops. This explains why the near-surface relative occurrence frequency over 10 dBZ in the simulation is higher than observed (Figures 2e and 2f). However, it is important to keep in mind that the Doppler radar was not on a

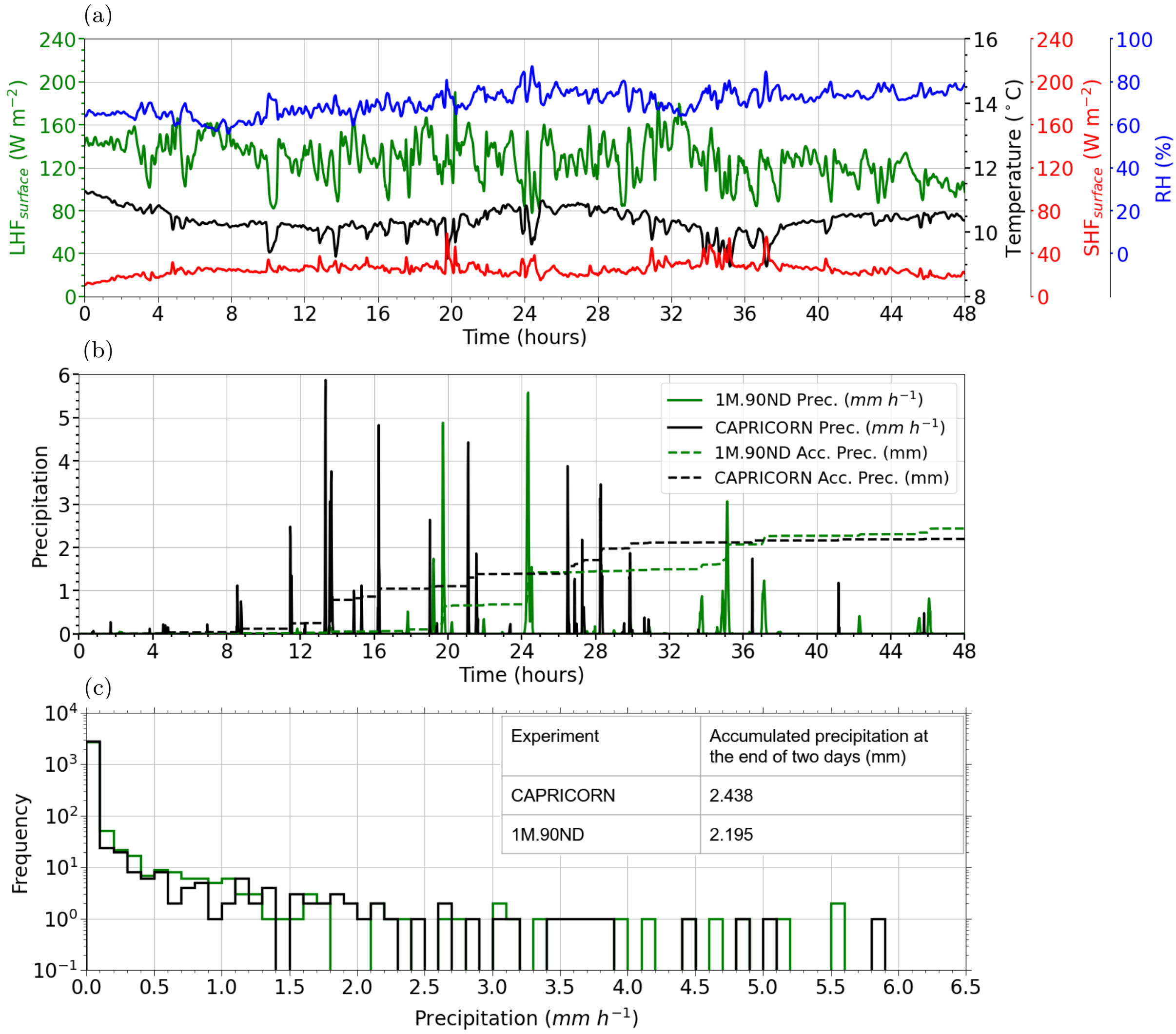

Figure 3: Time series of (a) LHF, SHF, temperature, and relative humidity for simulation, (b) simulated and observed surface precipitation rate (mm h^{-1}). (c) Histograms of precipitation rate for CAPRICORN (black) and simulation (green) along ship track. LHF, latent heat flux. SHF, sensible heat flux. The simulated data corresponds to the control simulation with a 1-min temporal resolution. Simulation period: 26th of March 2016 at 00:00:00 UTC to 28th of March 2016 at 00:00:00 UTC. Prec., precipitation rate; Acc. Prec., accumulated precipitation.

stable platform, which means that the observed MDV may be subject to greater uncertainty.

Although the reflectivity plots and CFADs provide insight into the microphysics of clouds and precipitation of the sampled SO stratocumuli, a statistical analysis of reflectivity that describes the intensity and duration of cloud-precipitation events can help us understand them better. Figures 4a to 4d show the fraction of cloud-precipitation events along the ship track categorized based on reflectivity between -20 and 20 dBZ incremented by a step of 10 dBZ. The fraction is calculated as the ratio of the duration of events in a reflectivity range to the total duration of cloud-precipitation events along the entire ship track. While lines and shading characterize the average intensity and duration of events, the distribution of individual dots (Figure 4e to 4h) characterizes the variability of those cloud-precipitation events. The observed lower reflectivity events (Figures 4a and 4b) dominate the cloud layer,

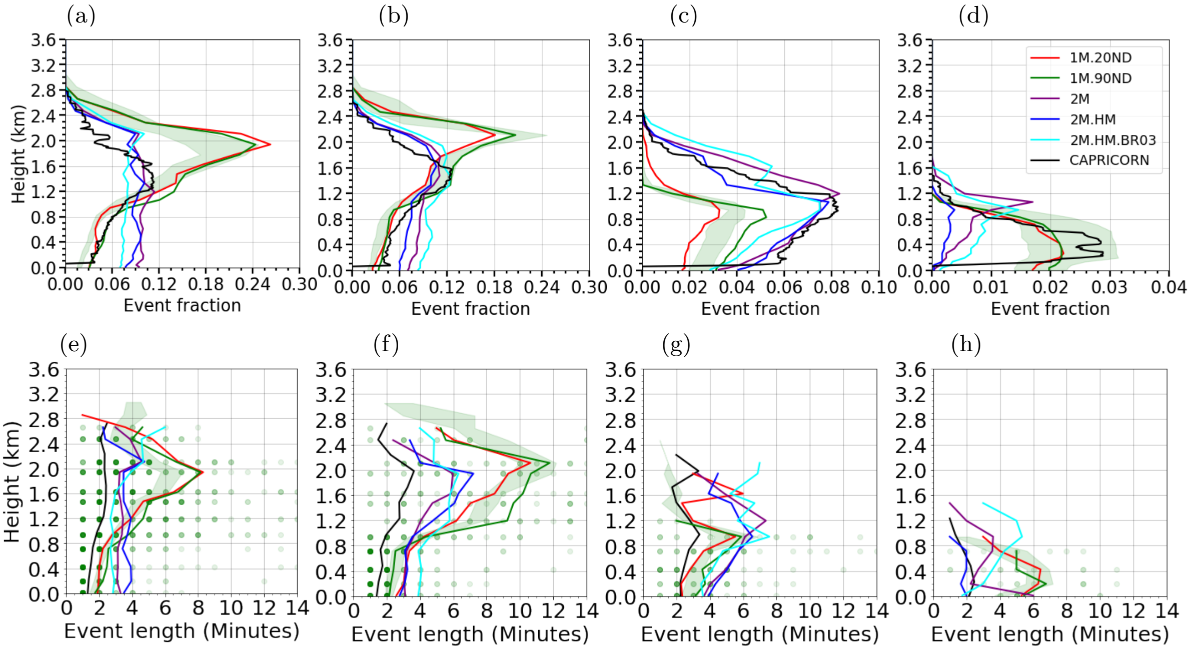

Figure 4: The cloud-precipitation occurrence (event) fraction (also termed as cloud cover) with height is categorized into reflectivity from (a) -20 to -10 dBZ, (b) -10 to 0 dBZ, (c) 0 to 10 dBZ and (d) 10 to 20 dBZ. The scatter plot represents the length of continuous cloud events with height, in the reflectivity range of (e) -20 to -10 dBZ, (f) -10 to 0 dBZ, (g) 0 to 10 dBZ and (h) 10 to 20 dBZ, where the lines represent the mean length of continuous cloud events in minutes (scatter mean). The scatter points (which are shown for control simulation only) become darker as the overlay of the data increases. The green shading corresponds to the quasi-ensemble variability (interquartile range) for the control simulation. This analysis takes into account the data throughout the ship track for the entire case period. The legends in 4d are common for all the subfigures.

as smaller hydrometeors (both liquid and ice) are captured in these reflectivity ranges. In a subsaturated environment, the smaller raindrops (ice crystals) evaporate (sublimate) efficiently since the surface-to-mass ratio is higher when compared with the larger raindrops (ice crystals). Since larger raindrops have higher reflectivities than solid hydrometeors (where both of them are equal in size), they are recorded in the highest reflectivity range (Figure 4d).

Similar distinct intermittent cloud events are simulated in 1M.90ND as were observed by the BASTA radar. However, the frequency of cloud events (Figure 4a and 4b) and their continuous duration (Figures 4e,4f) between -20 and 0 dBZ are overestimated above the melting level (approximately 1.2 km in altitude). The figures show that larger raindrops and graupel (between 0 and 10 dBZ) persist on far more successive timestamps than observed (Figure 4g), but are sparsely distributed (Figure 4c). Table S1 summarizes the range of simulated reflectivities for each hydrometeor. The simulated radar reflectivities >10 dBZ are solely due to larger raindrops. In this reflectivity range, the number of events that occur along the ship track is underestimated by 26% below 0.8 km altitude, although their mean event length is 3 times longer (Figures 4d and 4h).

3.2 Microphysical Sensitivities

We performed bulk microphysics sensitivity experiments to investigate the shortcomings of the control simulation (1M.90ND) with respect to the cloud microphysical processes, cloud occurrence, and surface precipitation. The reflectivity cross-section of the control simulation generates homogeneous clouds with constant CTHs after 36 hours of simulation time that were not observed (Figures 2a and 2b). This observed variability in CTH from 36 hours onward is qualitatively better captured in all 2M simulations (Figure 2a and Figure S8). The 1M simulation with reduced CDNC to 20 cm^{-3} qualitatively agrees with the arc structure of the observed CFAD (Figure 5a), however the bridge reflectivity (sum of reflectivity samples between -25 to 0 dBZ; 1.6 to 2 km altitude) reduces by 5% (Table S1c), and the bridge shifts to the left. The reduced CDNC experiment results in a decline in cloud water reflectivity and an increase in raindrop reflectivity in the CFAD bridge (Table S1). This is due to an inverse Twomey effect where the reduced CDNC leads to larger cloud droplets and more effective autoconversion. Meanwhile, it has also reduced the graupel reflectivity by 5.1%. Surprisingly, all the state-of-the-art 2M microphysics sensitivity experiments fail to achieve

dBZ	Statistics	CAP	1M.20ND	1M.90ND (ctrl)	2M.P	2M.HM	2M.HM.BR03
-40 to 20	EF	0.36	0.60	0.60	0.41	0.37	0.38
	MEL	9.10	45.41	41.33	21.25	22.0	22.92
-20 to -10	EF	0.11	0.26	0.24	0.11	0.10	0.10
	MEL	2.42	8.3	8.15	3.25	3.49	3.93
-10 to 0	EF	0.13	0.18	0.21	0.11	0.11	0.12
	MEL	2.77	9.30	10.67	5.98	7.21	6.32
0 to 10	EF	0.08	0.03	0.05	0.08	0.08	0.07
	MEL	2.0	3.0	2.0	3.29	4.5	6.88
10 to 20	EF	0.03	0.02	0.02	0.02	$<$0.01	0.01
	MEL	1.0	3.0	5.0	1.0	1.0	3.0

Table 2: Reflectivity statistics derived from Figure 4. 'EF' is the event fraction of the simulations and CAPRICORN at the altitude where their maximum event fraction occurs. 'MEL' is the mean event length (min) of the simulations and CAPRICORN at the altitude where the maximum event fraction of the respective simulation and CAPRICORN occurs. CAP, CAPRICORN. ctrl, control simulation.

the CFAD reflectivity arc, which is a proxy for cloud-precipitation vertical structure. The mean contribution of the graupel bridge reflectivity is reduced by 80% for 2M microphysics experiments and the mean increase in graupel for the experiments with secondary ice processes is just 23% with respect to 2M.P. Irrespective of the increase in rain and snow reflectivities in all 2M simulations, the reflectivity of the bridge is reduced by 46% (49%) with respect to the control simulation (BASTA radar). This demonstrates the importance of graupel processes in the SO mixed-phase Sc clouds sampled during CAPRICORN. The variations in hydrometeors other than graupel in the bridge are also noticeable, although the largest value of total graupel reflectivity due to its size and number concentration makes it dominant in the cloud layer (Table S1b). Meanwhile, the 2M.HM simulation generates very small cloud particles as their maximum reflectivity is 2.6 times less than the control simulation (Figure 2f and 5c).

In Table 2, the mean event (cloud-precipitation) length and the occurrence fraction have been derived for all experiments at the altitude of their maximum mean event fraction. All simulated values are overestimated. However, the 2M experiments show a better agreement with the observations than the 1M simulations. For all simulations, this agreement does not hold true across all altitudes. This shows that the microphysics of ICON simulations (1M and 2M) do not perfectly replicate the observed cloud vertical structure along the ship track. Figure 6 shows the simulated and observed surface precipitation along the ship track for the entire case period. All simulations except 2M.HM.BR03 show intense precipitation, hence the change in the accumulated precipitation in 2M.HM.BR03 is gradual at all timestamps. As expected, none of the experiments replicate the timing of the precipitation rate, the profile and variability of accumulated precipitation as compared to the observation. Although all the single track simulated data (except 2M.HM.BR03) overestimate the accumulated

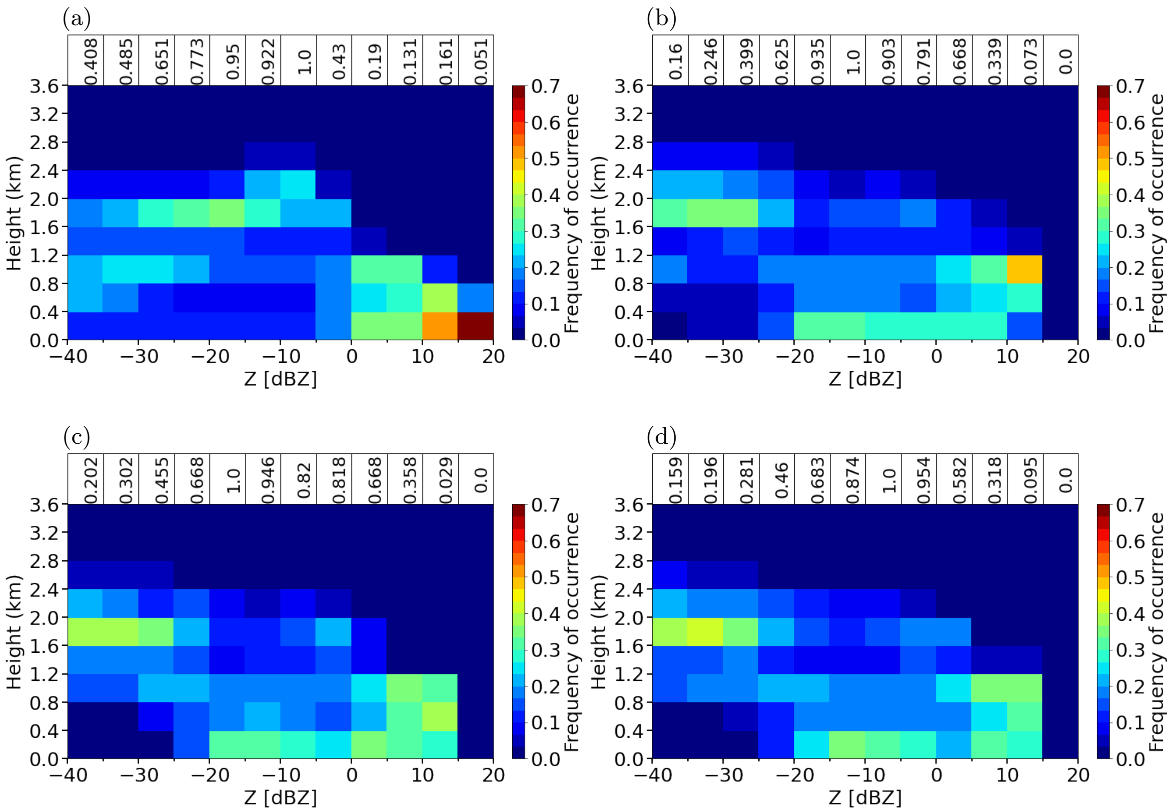

Figure 5: Contoured frequency by altitude diagrams (CFAD) with 1-min temporal resolution for the entire case study period of a) 1M.20ND, (b) 2M.P (c) 2M.HM and (d) 2M.HM.BR03. CFAD is normalized with the total samples in every reflectivity bin. The numerical data at the top of CFAD are the ratios of cumulated samples in every reflectivity bin to the highest cumulated samples from all the reflectivity bins. Case study period: 26$^{\text{th}}$ of March 2016 at 00:00:00 UTC to 28$^{\text{th}}$ of March 2016 at 00:00:00 UTC.

precipitation along the ship track at the end of two days, the ensemble accumulated precipitation variability (interquartile range) for 1M.90ND (the full variability is available only for 1M.90ND due to output limitation) increases with time, and further overlaps with that of other experiments (in particular during a large time period on 27$^{\text{th}}$ of March 2016). While the observations are entirely within the spatio-temporal variability of 1M.90Nd, a maximum of 66% for 2M.P and a minimum of 21% for 2M.HM.BR03 overlap with the variability of 1M.90ND. This suggests that due to the small sample size (two-day) and wide confidence interval (provided the ensemble variability within each experiment is significant), it remains difficult to characterize the full spatio-temporal variability of the surface precipitation.

The simulated domain mean surface precipitation (domain mean CB precipitation rates) are 0.045 mm hr^{-1} (3.6 mm hr^{-1}) for 2M.P, 0.053 mm hr^{-1} (3.3 mm hr^{-1}) for 2M.HM, and 0.061 mm hr^{-1} (2.7 mm hr^{-1}) for 2M.HM.BR03. This shows that despite a mean increase in total ice number concentration by two (three) orders of magnitude for 2M.HM (2M.HM.BR03) compared with 2M.P (Figure S9), the mean surface precipitation rate only modestly increases, and the CB precipitation rate even decreases. This result is somewhat counter-intuitive as one would expect increased cloud glaciation due to increased ICNC and thus increased growth rates by deposition (e.g. Vergara-Temprado et al. (2018)). Yet, CB precipitation rates decrease in our simulations. We cannot uniquely identify what is causing this decrease by 6% in 2M.HM and 23% in 2M.HM.BR03 with respect to 2M.P. However, the following processes may play a role. Firstly, the rate of ice hydrometeor growth through riming with cloud droplets is decreased in 2M.HM.BR03 which further reduces CB precipi-

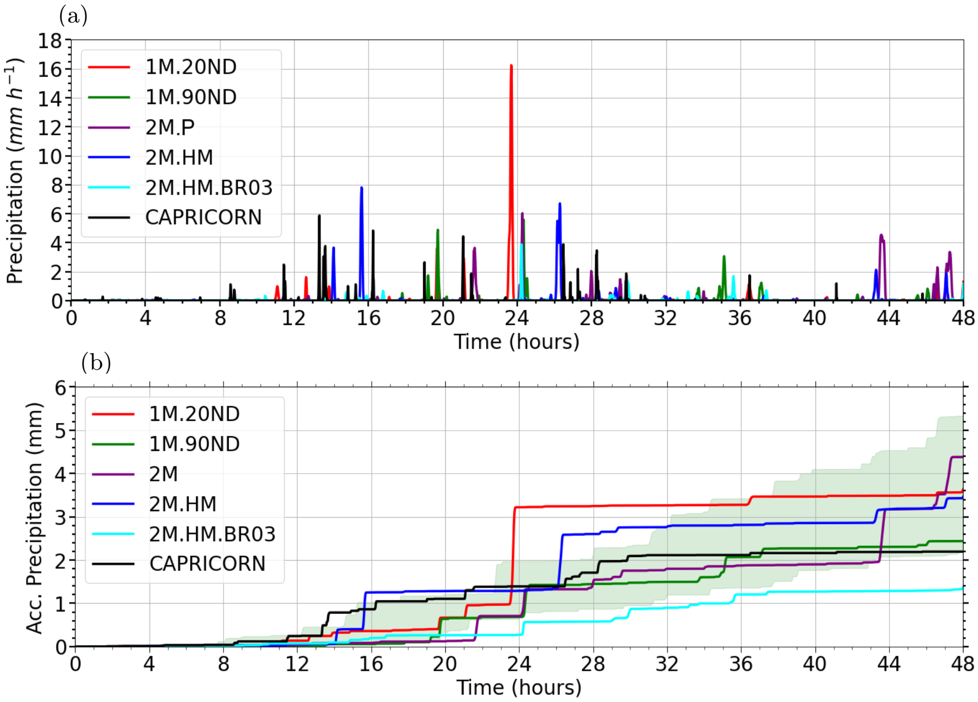

Figure 6: Time series of simulated and observed (a) precipitation rate (mm h^{-1}) and (b) accumulated precipitation (mm). Simulated data corresponds to control simulation and all the simulations in the bulk microphysical sensitivity analysis. The green shading corresponds to the quasi-ensemble variability (25$^{\text{th}}$ and 75$^{\text{th}}$ percentiles) of accumulated precipitation for the control simulation.

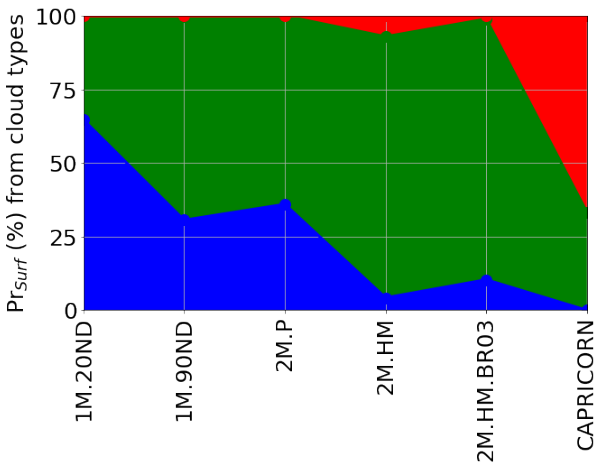

Figure 7: The relative percentage contribution of various cloud types (liquid - blue, mixed - green and ice - red) to surface precipitation along the ship track is stacked on top of one another. Data is analyzed for the entire case study period (26$^{\text{th}}$ of March 2016 at 00:00:00 UTC to 28$^{\text{th}}$ of March 2016 at 00:00:00 UTC).

tation (Figure S10). Secondly, the very small ejected ice crystals during collisional breakup may not be favorable for the formation of snow (ice-ice aggregation) and growth of snow (ice-snow collision). Thirdly, unlike HM, collisional breakup reduces the size and eventually the mass of individual solid hydrometeors by ice fragmentation, thus reducing their terminal fall velocity. Fourthly, while depositional growth increases, it does not compensate for the decrease in size by fragmentation. Thus terminal fall velocity remains low. It is likely that combined effect of: reduced terminal fall speed of ice crystals, and decreased riming efficiencies, reduce the mean CB precipitation rate in 2M.HM.BR03 as compared to 2M.HM.

Figure 7 shows the simulated cloud type contribution to surface precipitation rates. Here, the cloud types are categorized as liquid (liquid CB with liquid CB precipitation), ice (ice CB with ice CB precipitation), and mixed (CB and CB precipitation having different phases). The Twomey effect is illustrated clearly by the drop of 29% in liquid cloud contribution to precipitation rates between 1M.20ND and 1M.90ND. The ice (mixed) clouds contribute 67% (33%) to the observed precipitation rates, and the impact of ice (mixed) clouds on all the simulations is lower (higher). Ice and mixed-phase clouds account for an increase of 32% in surface precipitation rates from 2M.P to 2M.HM, but this fraction decreases by 6% from 2M.HM to 2M.HM.BR03. The fractional decline could be explained by the fact that (i) smaller ice particles require less latent heat to melt, as they cross the melting line within the cloud layer and (ii) reduced ice mass sedimentation as stated in the previous paragraph.

3.3 Impacts on Radiation

Figure 8a shows the observed and simulated surface downwelling SW radiation ($SW_{surf,down}$), as well as the liquid, mixed, and ice CT fractions. In general, we find that the lower the combined liquid and mixed CT fraction, the higher the mean $SW_{surf,down}$ is in all the simulations. This is entirely consistent with the larger scattering efficiency of the far more numerous and smaller cloud droplets as compared the few and large ice crystals (Greenwald et al., 1995). We further observe that changes in cloud phase area fraction have a considerably larger impact on $SW_{surf,down}$ than microphysical effects such as Twomey. An increase in ice-phase fraction in 2M.HM.BR03 with respect to 2M.HM increases $SW_{surf,down}$ by $8\,W\,m^{-2}$. This is twice as large as the decrease through the Twomey effect by $4\,W\,m^{-2}$ between 1M.20ND and 1M.90ND. Hence, these two simulations (2M.HM and 2M.HM.BR03) generate optically thicker clouds. In all other simulations the underestimation in $SW_{surf,down}$ is likely caused by both: an overabundance of liquid-containing clouds and overestimated optical depth.

As discussed above, CTP plays a predominant role in constraining the cloud-top radiative effect. The histograms of relative occurrences of CTP binned into 5°C CTT are shown in Figure 8b. The sampled open-cell (36 hours from 26th of March 2016 at 06:00:00 UTC) CTP from HIMAWARI along the ship track is classified with 78.3% as liquid. The total liquid fraction consists of 49.8% warm liquid water (LW) and 28.5% SLW. Meanwhile, merely 5.9% of all clouds in the control simulation are classified as liquid at CT with 1.1% LW and 4.8% SLW. The narrowly distributed simulated CTT with the mode between -10°C and -5°C holds 75.6% mixed-phase CTs against the observed 3.1%. Further, HIMAWARI classifies only 8.5% as mixed-phase open-cell stratocumuli at CT along the ship track, whereas 87.78% are identified as such in the control simulation. This may be due to the lower vertical resolution, inadequate representation of CT turbulence, dissipation of the sharp temperature inversion due to TKE centered around the CT instead of being at or below the CT, poor updraft velocity to push cloud droplets to the CT (Vignon et al., 2021), and possibly overprediction of ICNC by the temperature-dependent Cooper parameterization for ice nucleation (Cooper, 1986). No open-cell Sc CTTs are simulated (1M.90ND) below -15°C and above 5°C, whereas 13.1% (ice) and 21.8% (LW) CTs were observed below and above these limits along the ship track. However, the warm clouds in HIMAWARI may be subject to large uncertainties since the surface temperature and emissivity influence the CTT retrievals (Huang et al., 2019). Overall, the control simulation along the ship track (open-cell period) overestimates the liquid and mixed-phase CTs by 35.2%, and overestimates the cloud occurrence by 26.1%, resulting in the underestimation of surface downwelling SW radiation by 42.7%, compared to the observations.

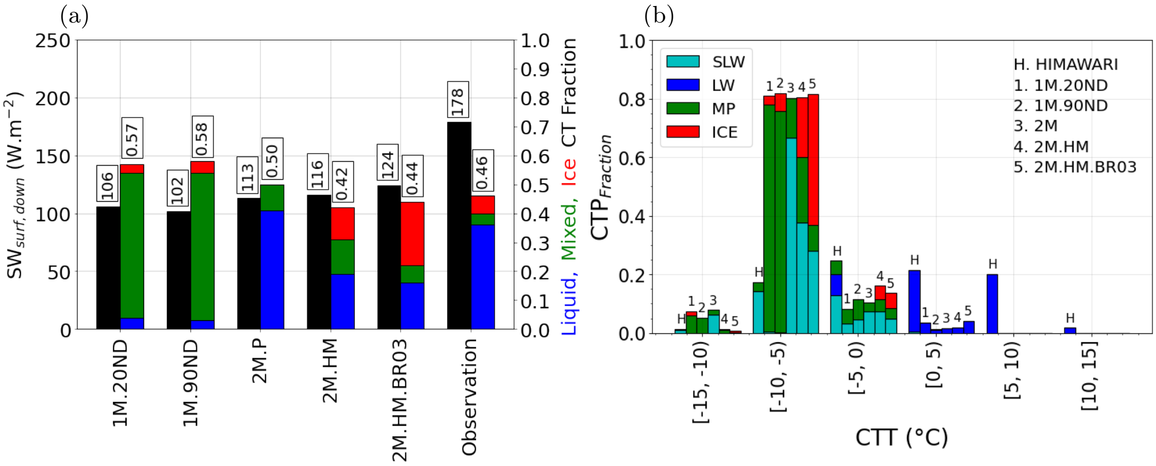

Figure 8: HIMAWARI and simulated data along the ship track during the open-cell period. (a) Surface downwelling shortwave radiation (W m^{-2}) and the total CT fractions with relative contributions of liquid (blue), mixed (green), and ice (red) phase (stacked one over the other). (b) Histograms of CTP fractions as a function of the cloud-top temperature (CTT) with the bins of 5°C. CT, cloud-top. HIMAWARI data is obtained from Huang et al. (2019); Lang et al. (2021).

Although the CTP distinguished with CTT doesn't vary substantially for the reduced CCN experiment (1M.20ND), the occurrence of SLW significantly increases in the 2M experiments between -10°C and -5°C (Figure 8b). Since many cloud event streaks are entirely liquid with no traces of solid hydrometeors (Figure S11), they increase the CT SLW fraction. As opposed to the Cooper ICNC curve, the observationally constrained INP immersion freezing parameterization with considerably lower INP background concentrations has produced MPCs only at a few instances along the ship track. Although, the in-cloud domain mean IWP has increased to 50 g m^{-2} in the 2M.P simulation (Figure S9). This shows that the immersion INP parameterization adjusted for the SO remote region is insufficient to reduce cloud-radiative biases caused by inaccurate representations of cloud phase and the partitioning of the total water path between LWP and IWP. Similar to the control simulation, all the sensitivity experiments cluster 80% of the simulated CTs between -10°C and -5°C. Warm CTs above 5°C are still missing. However, the increase in the ice occurrence fraction at CT is consistent with the activation of secondary ice processes between -10°C and -5°C (2M.HM and 2M.HM.BR03).

3.4 Perturbed-Parameter Experiments to enhance graupel formation in 2M simulations

As discussed in section 3.2, the state-of-the-art 2M microphysics scheme in ICON displays stronger biases in the vertical structure of precipitation than the 1M simulations. Here, we look at the microphysical pathways to understand the role of individual processes for both schemes in detail (Figure 9). As discussed earlier, graupel particles play a significant role in the occurrence of the bridge in the cloud layer in CFAD diagrams. The time-height cross-section of the simulated phase shows that graupel (hatching in figures) covers a larger sample in 1M (Figure 2d and Figure S11a) than in all the 2M simulations (Figures S11b to S11d) above the melting level. The 1M and 2M microphysical pathway analysis discussed in this section is obtained from the 1M.90ND and 2M.HM simulations on 27th of March 2016. Among the graupel growth processes shown in Figure S12 and Figure 9, CG2G_rim (cloud-graupel to graupel riming) and RG2G_rim (rain-graupel to graupel riming) are the dominant processes. The CG2G_rim process rate is higher in the cloud layer in the 1M scheme (9.13) than in the 2M scheme (2.30). Note that all process rates are normalized for comparability by WVL as described in section 2.3 and are thus unitless. Although RG2G_rim is not

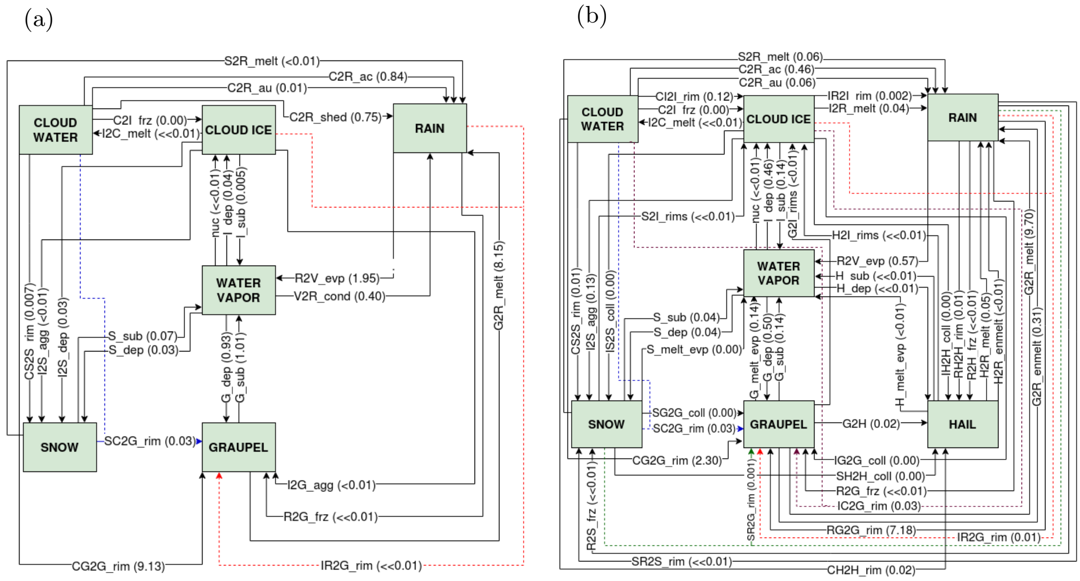

Figure 9: Flowchart of the microphysical processes on 27$^{\mathrm{th}}$ of March 2016 for (a) 1M.90ND, (b) 2M.HM. The ratios of each microphysical process rate to the rate of total water vapor loss (WVL) are shown within parenthesis (refer to equations 1 and 2). The abbreviations are as follows: C, cloud ice. I, cloud ice. R, Rain. S, snow. G, graupel. H, hail. V, vapor. au, autoconversion. ac, accretion. frz, freezing. melt, melting. shed, shedding. evp, evaporation. cond, condensation. sub, sublimation. dep, deposition. rim, riming. rims, rime splintering. coll, solid hydrometeor collision. agg, aggregation. nuc, ice nucleation.

parameterized in the 1M scheme, the cloud phase time series indicates larger traces of raindrops in the cloud layer in 2M scheme (Figures S11b-d) than in 1M scheme (Figure 2d and Figure S11a). This might be because CG2G_rim in the 1M scheme is more efficient in scavenging cloud droplets before they grow into raindrops than the CG_rim and RG_rim rates in 2M scheme. All graupel formation processes (such as cloud-snow to graupel, ice-rain to graupel, rain-snow to graupel, rain to graupel freezing, and ice to graupel by aggregation) are associated with a lower mass transfer to the graupel category than graupel growth processes (i.e. CG2G_rim and R2G2G_rim). Figures 5b to 5d show strong near-surface high reflectivity bands (-20 dBZ to 15 dBZ) with the higher relative frequency of occurrences in the 2M simulations. However, this was not observed during CAPRICORN and not simulated in the 1M scheme. Possible reasons could be a higher (lower) graupel melting rate of 9.70 (8.15), a lower (higher) raindrop evaporation rate of 0.57 (1.95), and lower (higher) graupel sublimation rate of 0.14 (0.93) for 2M.HM (1M.90ND) (Figure 9).

As a result, raindrop selfcollection may be effective in 2M.HM, which enhances droplet diameter and further increases cloud reflectivity. Among the microphysical processes shown in the flow chart of microphysical pathways, graupel melting is the major source of rain in both schemes for SO Sc clouds. Graupel melting accounts for about 80% of the rain in the 1M scheme and 91% of the rain in the 2M scheme. Furthermore, 24% and 6% of the melted graupel evaporate in 1M and 2M microphysics schemes respectively. Although the new rain particle formation in the cloud layer by autoconversion is larger by a factor of 6 in the 2M scheme, their growth by accretion is reduced by a factor of 2. Hence, the raindrops in the cloud layer might not be large enough to get rimed by graupel. Most raindrops are scavenged in the riming processes in 1M simulations, making it difficult to verify this hypothesis with the existing set of simulations. Thus, we performed further sensitivity experiments (summarized in Table 1) altering parameters affecting graupel generation and growth, either directly, or indirectly to further understand the deficiencies of the simulated vertical structure of precipitation in the 2M simulations.

Expt No.	Description	CG2G _rim	G2R _melt	RG2G _rim	G _dep	G _budget
1	2M.HM * E10	24.80	-108.06	77.52	5.41	9.00
2	2M.P	-14.37	-16.46	-12.09	-31.41	-19.47
3	2M.HM.BR03	5.12	6.75	5.28	1.35	6.08
4	CCN10	-1.09	-8.57	-9.60	-11.59	-7.54
5	CCN1000	-39.71	-45.93	-49.67	-34.84	-41.79
6	aukcc*0.5	2.32	3.88	4.37	0.88	0.72
7	aukcc*2	-1.23	-5.95	-6.91	-1.24	-0.55
8	ice_vel_coef	3.85	-4.04	-5.63	-2.83	-0.32
9	rain_atlas	-6.90	-4.87	-3.59	-3.96	-6.25
10	agg_50	1.45	0.94	1.10	0.53	0.99
11	agg_200	-4.41	-2.17	-2.97	-3.64	-2.61
12	gr_d_m	-7.90	-8.53	-9.65	-7.08	0.96
13	gr_d_h	-16.56	-21.51	-24.15	-2.76	5.61
14	gr_v_h	-3.29	-9.28	-12.13	-38.94	-51.70
15	gr_max_dia	-63.85	-76.84	-81.73	-59.72	-60.49

Table 3: The top row (in kg) shows the sum of the product of hourly process rates and volume of each cell for the reference simulation (2M.HM) on 27th of March 2016. G_budget (in kg) for the reference simulation refers to the sum of the product of instantaneous graupel mass density and the volume of each cell. All the other rows are percentage changes with respect to the reference simulation. The intensity of the color scale shows the percentage decrease (increase) in red (blue). The table only shows process budgets that exceed 50% of the G_budget.

To realistically simulate the graupel processes in the SO Sc clouds, it is crucial to analyze their sensitivity to the parameters related to CCN and ice-phase processes. Our small parameter ensemble is motivated by the importance of CG2G_rim and RG2G_rim for graupel growth. CCN concentrations are perturbed for the former, and the rain terminal velocity relation (power-law (Seifert & Beheng, 2006), and atlas-law (Seifert et al., 2014)), as a function of its mass, is perturbed for the latter. As reported in Seifert and Beheng (2006), the velocity coefficients of ice crystals are based on the measurements from Locatelli and Hobbs (1974); Heymsfield and Kajikawa (1987). Furthermore, the graupel density and its velocity measured during the winter months of 1971-1972 and 1972-1973 in the Cascade Mountains of Washington (Locatelli & Hobbs, 1974) are used to study the sensitivity of the G_budget.

The 2M.HM simulation (Table 3) is considered a reference experiment in this section. The numbers, except for the G_budget in the reference experiment, are averaged hourly and summed over a time period of 24 hours on 27th of March, 2016. The G_budget in the last column of this experiment refers to the time-space integrated sum of instantaneous hourly graupel mass mixing ratios for the same 24 hours period. All the other rows in this table represent the percentage change with respect to the reference simulation. The increase in CCN from 10 cm^{-3} to 1000 cm^{-3} results in a monotonic increase in smaller cloud droplets (Twomey & Warner, 1967). This reduces the cloud droplet autoconversion and accretion rates, and further delays the rain to graupel riming process. The net G_budget is reduced by 41.79%. Similarly, reducing the CCN (CCN10) below a threshold value also reduces the G_budget and the related process rates. A reduced autoconversion kernel coefficient by a factor of 2 increased the rate of the cloud-graupel riming process by 2.3%, since the rain particle formation slowed down. This modest increase could be attributed to the lower cloud liquid water path (LWP) in 2M simulations compared to 1M simulations. Any increase in graupel density allows for an increase in its mass and hence a modest gain in the G_budget. However, the mass and terminal velocity of the hydrometeors are coupled by a power-law. An increase in graupel density or graupel diameter increases the terminal velocity which reduces its residence time, and hence the G_budget (experiments 13 and 14 in Table 1). The rime splintering process reduces the gap between the simulated and observed ICNC, and also governs the new graupel particle formation processes (experiment no. 15 in Table 1) in the remote environment of the SO boundary layer. Hence, the secondary ice production processes (HM and collisional breakup) lead to an increase in the net G_budget.

Overall, it is significant that (i) the CCN number concentration affects the G_budget through the RG2G_riming process and (ii) the graupel properties (density, velocity, and size) have a strong effect on the net G_budget. The 2M microphysics sensitivity experiments for SO Sc clouds show that the net G_budget is at its maximum when: (i) the graupel density, velocity, and size are low, (ii) the power-law captures the raindrop velocity as a function of its mass, (iii) secondary ice production processes are active, and (iv) CCN values are low.

4 Discussion and Conclusions

We have evaluated the ability of kilometer-scale ICON real-case simulations against the observed cloud and precipitation statistics derived from remote sensing and in-situ measurements during CAPRICORN. In general, the control simulation captured the observed cloud-precipitation vertical structure due to graupel growth by the riming of cloud droplets. A continuous formation of graupel, its growth in the cloud layer, and subsequent melting are crucial processes for realistically representing the cloud-precipitation vertical structure of SO Sc clouds. Further, a lower CCN concentration and increased density, velocity, and size of graupel particles all enhance low-cloud graupel formation. According to the microphysical pathway analysis, graupel melting is a major source of SO Sc precipitation during CAPRICORN. The duration of continuous cloudy elements containing either cloud droplets, rain, or graupel particles is overestimated in all ICON simulations. This results in an overestimated mean duration of cloudy elements along the entire ship track. Thus, the timing of the simulated cloud-precipitation events doesn't agree with CAPRICORN, which is also evident in the comparison with observed surface precipitation rates. The simulated surface precipitation is sparsely dispersed, whereas the OceanRAIN disdrometer measures densely distributed precipitation rates with relatively sharp spikes. Although the simulated accumulated precipitation at the end of two days is closer to CAPRICORN, the onset of stronger precipitation in the open-cell region is delayed by 9 hours in the simulation. Although the observations are within the simulated range of variability of the control simulation, longer continuous observations within the same cloud regime would be needed to fully constrain the simulated cloud-precipitation statistics. Despite these shortcomings, the control simulation captured the surface cold pool (drop in near-surface air temperature) in many timestamps that favored the occurrence of the transition layer and the decoupling of the boundary layer.

The phase distinction from the merged radar-lidar product, the CFAD of radar reflectivity, and the HIMAWARI CTP confirm the presence of ice in the cloud. We observed that the bridge reflectivity (reflectivity of a sharp horizontal band in the arc i.e., in the cloud layer) is a reasonable proxy for evaluating the cloud layer hydrometeors. According to the independent hydrometeor reflectivity contribution analysis for all simulations, a relative increase in the graupel mass in the cloud layer reduced the gap between the observed and simulated bridge reflectivities, resulting in a more realistic representation of the arc structure. The highest contribution of graupel is 66% (1M.90ND) and 59% (1M.20ND) in 1M simulations that realistically represent the observed cloud vertical structure, while it is less than 20% in 2M simulations. In addition to the occurrence of graupel in the cloud layer, all other processes involving graupel and raindrops, such as partially sublimated frozen particles, partially evaporated larger raindrops, melting of graupel, raindrop selfcollection, and solid hydrometeors coated with liquid layer during the collision of ice particles with raindrops are also crucial in describing the observed cloud-precipitation vertical structure. The raindrops in the cloud layer (bridge) dominate the reflectivities rather than the graupel in all 2M simulations. The enhanced raindrop reflectivity in the cloud layer did not increase bridge reflectivity, rather, the bridge reflectivity decreased by 46% compared to the control simulation. Theoretically, graupel (rain) contributed reflectivities could be increased (decreased) if efficient in-cloud graupel growth by riming rain scavenges raindrops. Hence, the bridge statistics clearly emphasize the significance of graupel in SO Sc clouds.

The presence of graupel, which is one of the necessary conditions in HM (Hallett & Mossop, 1974) and an enhancing parameter due to increased collisional kinetic energy in breakup collisions (Phillips, Yano, & Khain, 2017), increases the secondary ice production. We investigated the sensitivity with respect to secondary ice generating processes (HM and collisional breakup) in Sc clouds during CAPRICORN. The maximum reflectivity of cloud droplets in the 2M.HM simulation is 2.6 times lower than the control simulation, indicating that cloud droplet size decreased. The reflectivity event fractions of all the 2M simulations show that the larger raindrops (20> dBZ>10) evaporate effectively in the sub-cloud layer and increase the smaller raindrop number concentration in the intermediate reflectivity range (10> dBZ>-20), and hence the occurrence of strong frequency of occurrence band near the surface in the 2M CFAD diagrams. This indicates that the near-surface raindrops in all 2M simulations are smaller compared to 1M simulations. Although the domain mean total ice number concentration (total ice water path) in 2M.HM.BR03 increase by roughly 10 (1.4) times compared to 2M.HM, the domain mean precipitation increases by just 1.2 times. Hence, despite the increase in the total ice number concentration through collisional breakup, the precipitation statistics remain dominated by melted graupel containing primary INP along the ship track.

The $SW_{\mathrm{surf,down}}$ along the ship track in the control simulation is negatively biased by 43% due to the overestimation of the liquid and mixed-phase CT by 35%, and the cloud occurrence by 26%. Furthermore, the $SW_{\mathrm{surf,down}}$ of all simulations is negatively biased irrespective of the extent of liquid CT fraction, yet, most of the simulated total liquid and mixed-phase CT fractions are higher than observed during CAPRICORN. The control simulation failed to produce the dominant liquid CTs, instead, 87.78% are mixed-phase with just 8.5% diagnosed as such in HIMAWARI retrievals. This could be due to a variety of factors, one of which is the insufficient vertical resolution in all simulations that would be required to fully represent a supercooled liquid layer on top of the mixed-phase cloud. It is worth noting that the 2M simulations (2M.HM and 2M.HM.BR03) adjusted for a remote INP environment over the SO generate optically thicker clouds, as primary nucleation is considerably reduced and indeed many cloud profiles are entirely liquid. All other simulations generate positively biased cloud cover and/or optically thicker clouds. Thus the cloud radiative bias in this particular regime is contrary to the climatological bias (Trenberth & Fasullo, 2010; Bodas-Salcedo et al., 2014; Vergara-Temprado et al., 2018).

References

Ahn, E., Huang, Y., Chubb, T. H., Baumgardner, D., Isaac, P., de Hoog, M., ... Manton, M. J. (2017). In situ observations of wintertime low-altitude clouds over the Southern Ocean. *Quarterly Journal of the Royal Meteorological Society*, *143*(704), 1381–1394. doi: 10.1002/qj.3011

Alexander, S. P., & Protat, A. (2018). Cloud Properties Observed From the Surface and by Satellite at the Northern Edge of the Southern Ocean. *Journal of Geophysical Research: Atmospheres*, *123*(1), 443–456. doi: 10.1002/2017JD026552

Bechtold, P., Köhler, M., Jung, T., Doblas-Reyes, F., Leutbecher, M., Rodwell, M. J., ... Balsamo, G. (2008, jul). Advances in simulating atmospheric variability with the ECMWF model: From synoptic to decadal time-scales. *Quarterly Journal of the Royal Meteorological Society*, *134*(634), 1337–1351. Retrieved from `https://onlinelibrary.wiley.com/doi/10.1002/qj.289` doi: 10.1002/qj.289

Bodas-Salcedo, A., Williams, K. D., Field, P. R., & Lock, A. P. (2012). The surface downwelling solar radiation surplus over the southern ocean in the met office model: The role of midlatitude cyclone clouds. *Journal of Climate*, *25*(21), 7467–7486. doi: 10.1175/JCLI-D-11-00702.1

Bodas-Salcedo, A., Williams, K. D., Ringer, M. A., Beau, I., Cole, J. N., Dufresne, J. L., ... Yokohata, T. (2014). Origins of the solar radiation biases over the Southern Ocean in CFMIP2 models. *Journal of Climate*, *27*(1), 41–56. doi: 10.1175/JCLI-D-13-00169.1

Bosello, F., Roson, R., & Tol, R. S. J. (2007, may). Economy-wide Estimates of the Implications of Climate Change: Sea Level Rise. *Environmental and Resource Economics*, *37*(3), 549–571. Retrieved from `http://dx.doi.org/10.1038/s41561-018-0234-1http://www.atmos.washington.edu/{~}sgw/PAPERS/2007{\_}ndp026e.pdfhttps://journals.ametsoc.org/doi/pdf/10.1175/1520-0477(1984)065{\%}3C1290:OFROSM{\%}3E2.0.CO{\%}3B2http://link.springer.com/10.1007/s10640-006-9048-5` doi: 10.1007/s10640-006-9048-5

Bretherton, C. S., & Wyant, M. C. (1997). Moisture transport, lower-tropospheric stability, and decoupling of cloud-topped boundary layers. *Journal of the Atmospheric Sciences*, *54*(1), 148–167. doi: 10.1175/1520-0469(1997)054⟨0148:MTLTSA⟩2.0.CO;2

Caughey, S. J., Crease, B. A., & Roach, W. T. (1982). A field study of nocturnal stratocumulus II Turbulence structure and entrainment. *Quarterly Journal of the Royal Meteorological Society*, *108*(455), 125–144. doi: 10.1002/qj.49710845508

Cooper, W. A. (1986, dec). Ice Initiation in Natural Clouds. *Meteorological Monographs*, *43*(43), 29–32. Retrieved from `https://journals.ametsoc.org/view/journals/amsm/21/43/0065-9401-21{\_}43{\_}29.xmlhttp://journals.ametsoc.org/doi/10.1175/0065-9401-21.43.29` doi: 10.1175/0065-9401-21.43.29

Delanoë, J., Protat, A., Vinson, J. P., Brett, W., Caudoux, C., Bertrand, F., ... Dupont, J. C. (2016). BASTA: A 95-GHz FMCW Doppler radar for cloud and fog studies. *Journal of Atmospheric and Oceanic Technology*, *33*(5), 1023–1038. doi: 10.1175/JTECH-D-15-0104.1

Demott, P. J., Prenni, A. J., McMeeking, G. R., Sullivan, R. C., Petters, M. D., Tobo, Y., ... Kreidenweis, S. M. (2015). Integrating laboratory and field data to quantify the immersion freezing ice nucleation activity of mineral dust particles. *Atmospheric Chemistry and Physics*, *15*(1), 393–409. doi: 10.5194/acp-15-393-2015

Doms, G., Förstner, J., Heise, E., Herzog, H.-J., Mironov, D., Raschendorfer, M., ... Vogel, G. (2011). A description of the Nonhydrostatic Regional COSMO Model, Part II: Physical parameterization. Deutscher Wetterdienst: Offenbach, Germany. *Www.Cosmo-Model.Org*(September), 152. doi: http://www.cosmo-model.org

Fiddes, S. L., Protat, A., Mallet, M. D., Alexander, S. P., & Woodhouse, T. (2022). Southern Ocean cloud and shortwave radiation biases in a nudged climate model simulation : does the model ever get it right ? *Atmospheric Chemistry and Physics Discussions*, *Preprint*(April), 1–34. Retrieved from `https://acp.copernicus.org/preprints/acp-2022-259/acp-2022-259.pdf`

Fridlind, A. M., Ackerman, A. S., McFarquhar, G., Zhang, G., Poellot, M. R., DeMott,

P. J., ... Heymsfield, A. J. (2007). Ice properties of single-layer stratocumulus during the Mixed-Phase Arctic Cloud Experiment: 2. Model results. *Journal of Geophysical Research Atmospheres*, *112*(24), 1–25. doi: 10.1029/2007JD008646

Greenwald, T. J., Stephens, G. L., Christopher, S. A., & Vonder Haar, T. H. (1995, dec). Observations of the Global Characteristics and Regional Radiative Effects of Marine Cloud Liquid Water. *Journal of Climate*, *8*(12), 2928–2946. Retrieved from `http://journals.ametsoc.org/doi/10.1175/1520-0442(1995)008{\%}3C2928:OOTGCA{\%}3E2.0.CO;2` doi: 10.1175/1520-0442(1995)008⟨2928:OOTGCA⟩2.0.CO;2

Hallett, J., & Mossop, S. C. (1974, may). Production of secondary ice particles during the riming process. *Nature*, *249*(5452), 26–28. Retrieved from `https://www.nature.com/articles/249026a0` doi: 10.1038/249026a0

Heymsfield, A. J., & Kajikawa, M. (1987, apr). An Improved Approach to Calculating Terminal Velocities of Plate-like Crystals and Graupel. *Journal of the Atmospheric Sciences*, *44*(7), 1088–1099. Retrieved from `http://journals.ametsoc.org/doi/10.1175/1520-0469(1987)044{\%}3C1088:AIATCT{\%}3E2.0.CO;2` doi: 10.1175/1520-0469(1987)044⟨1088:AIATCT⟩2.0.CO;2

Hu, Y., Rodier, S., Xu, K. M., Sun, W., Huang, J., Lin, B., ... Josset, D. (2010). Occurrence, liquid water content, and fraction of supercooled water clouds from combined CALIOP/IIR/MODIS measurements. *Journal of Geophysical Research Atmospheres*, *115*(19), 1–13. doi: 10.1029/2009JD012384

Hu, Y., Winker, D., Vaughan, M., Lin, B., Omar, A., Trepte, C., ... Kuehn, R. (2009). CALIPSO/CALIOP cloud phase discrimination algorithm. *Journal of Atmospheric and Oceanic Technology*, *26*(11), 2293–2309. doi: 10.1175/2009JTECHA1280.1

Huang, Chubb, T., Baumgardner, D., DeHoog, M., Siems, S. T., & Manton, M. J. (2017). Evidence for secondary ice production in Southern Ocean open cellular convection. *Quarterly Journal of the Royal Meteorological Society*, *143*(704), 1685–1703. doi: 10.1002/qj.3041

Huang, Siems, S., Manton, M., Protat, A., Majewski, L., & Nguyen, H. (2019). Evaluating himawari-8 cloud products using shipborne and CALIPSO observations: Cloud-top height and cloud-top temperature. *Journal of Atmospheric and Oceanic Technology*, *36*(12), 2327–2347. doi: 10.1175/JTECH-D-18-0231.1

Klepp, C. (2015). The oceanic shipboard precipitation measurement network for surface validation - OceanRAIN. *Atmospheric Research*, *163*, 74–90. Retrieved from `http://dx.doi.org/10.1016/j.atmosres.2014.12.014` doi: 10.1016/j.atmosres.2014.12.014

Lang, F., Huang, Y., Protat, A., Truong, S. C. H., Siems, S. T., & Manton, M. J. (2021). Shallow Convection and Precipitation over the Southern Ocean: A Case Study during the CAPRICORN 2016 Field Campaign. *Journal of Geophysical Research: Atmospheres*, 1–23. doi: 10.1029/2020jd034088

Locatelli, J. D., & Hobbs, P. V. (1974). Fall speeds and masses of solid precipitation particles. *Journal of Geophysical Research*, *79*(15), 2185–2197. doi: 10.1029/jc079i015p02185

Mace, G. G., Benson, S., & Hu, Y. (2020). On the Frequency of Occurrence of the Ice Phase in Supercooled Southern Ocean Low Clouds Derived From CALIPSO and CloudSat. *Geophysical Research Letters*, *47*(14), 1–8. doi: 10.1029/2020GL087554

Mace, G. G., & Protat, A. (2018a). Clouds over the Southern Ocean as observed from the R/V investigator during CAPRICORN. Part I: Cloud occurrence and phase partitioning. *Journal of Applied Meteorology and Climatology*, *57*(8), 1783–1803. Retrieved from `https://doi.org/10.1175/JAMC-D-17-0194.1` doi: 10.1175/JAMC-D-17-0194.1

Mace, G. G., & Protat, A. (2018b). Clouds over the Southern Ocean as observed from the R/V investigator during CAPRICORN. Part II: The properties of nonprecipitating stratocumulus. *Journal of Applied Meteorology and Climatology*, *57*(8), 1805–1823. doi: 10.1175/JAMC-D-17-0195.1

Mace, G. G., Protat, A., Humphries, R. S., Alexander, S. P., McRobert, I. M., Ward, J., ... McFarquhar, G. M. (2020). Southern Ocean Cloud Properties Derived from CAPRICORN and MARCUS Data. *Journal of Geophysical Research: Atmospheres*, 1–23. doi: 10.1029/2020jd033368

McCluskey, C. S., DeMott, P. J., Ma, P. L., & Burrows, S. M. (2019). Numerical Representations of Marine Ice-Nucleating Particles in Remote Marine Environments Evaluated Against Observations. *Geophysical Research Letters*, *46*(13), 7838–7847. doi: 10.1029/2018GL081861

McCluskey, C. S., Hill, T. C., Humphries, R. S., Rauker, A. M., Moreau, S., Strutton, P. G., ... DeMott, P. J. (2018). Observations of Ice Nucleating Particles Over Southern Ocean Waters. *Geophysical Research Letters*, *45*(21), 11,989–11,997. doi: 10.1029/2018GL079981

Mech, M., Maahn, M., Kneifel, S., Ori, D., Orlandi, E., Kollias, P., ... Crewell, S. (2020). PAMTRA 1.0: The Passive and Active Microwave radiative TRAnsfer tool for simulating radiometer and radar measurements of the cloudy atmosphere. *Geoscientific Model Development*, *13*(9), 4229–4251. doi: 10.5194/gmd-13-4229-2020

Mellor, G. L., & Yamada, T. (1982). Development of a turbulence closure model for geophysical fluid problems. *Reviews of Geophysics*, *20*(4), 851–875. Retrieved from `https://agupubs.onlinelibrary.wiley.com/doi/abs/10.1029/RG020i004p00851http://doi.wiley.com/10.1029/RG020i004p00851` doi: 10.1029/RG020i004p00851

Mlawer, E. J., Taubman, S. J., Brown, P. D., Iacono, M. J., & Clough, S. A. (1997). Radiative transfer for inhomogeneous atmospheres: RRTM, a validated correlated-k model for the longwave. *Journal of Geophysical Research D: Atmospheres*, *102*(14), 16663–16682. doi: 10.1029/97jd00237

Muhlbauer, A., McCoy, I. L., & Wood, R. (2014). Climatology of stratocumulus cloud morphologies: Microphysical properties and radiative effects. *Atmospheric Chemistry and Physics*, *14*(13), 6695–6716. doi: 10.5194/acp-14-6695-2014

Noh, Y. J., Miller, S. D., Heidinger, A. K., Mace, G. G., Protat, A., & Alexander, S. P. (2019). Satellite-Based Detection of Daytime Supercooled Liquid-Topped Mixed-Phase Clouds Over the Southern Ocean Using the Advanced Himawari Imager. *Journal of Geophysical Research: Atmospheres*, *124*(5), 2677–2701. doi: 10.1029/2018JD029524

Phillips, V. T., Yano, J. I., Formenton, M., Ilotoviz, E., Kanawade, V., Kudzotsa, I., ... Tessendorf, S. A. (2017). Ice multiplication by breakup in ice-ice collisions. Part II: Numerical simulations. *Journal of the Atmospheric Sciences*, *74*(9), 2789–2811. doi: 10.1175/JAS-D-16-0223.1

Phillips, V. T., Yano, J. I., & Khain, A. (2017). Ice multiplication by breakup in ice-ice collisions. Part I: Theoretical formulation. *Journal of the Atmospheric Sciences*, *74*(6), 1705–1719. doi: 10.1175/JAS-D-16-0224.1

Raschendorfer, M. (2001). The new turbulence parameterization of LM. *COSMO Newsletter No. 1*(February), 89–97. Retrieved from `ThenewturbulenceparameterizationofLM`

Riehl, H., Yeh, T. C., Malkus, J. S., & la Seur, N. E. (1951, oct). The north-east trade of the Pacific Ocean. *Quarterly Journal of the Royal Meteorological Society*, *77*(334), 598–626. Retrieved from `http://doi.wiley.com/10.1002/qj.49707733405` doi: 10.1002/qj.49707733405

Royer, P., Bizard, A., Sauvage, L., & Thobois, L. (2014). Validation protocol and intercomparison campaigns with the R-MAN 510 aerosol lidar. *Proc. 17th International Symposium for the Advancement of Boundary Layer Remote Sensing*(August), 1. doi: 10.13140/2.1.4778.1767

Sandu, I., & Stevens, B. (2011). On the factors modulating the stratocumulus to cumulus transitions. *Journal of the Atmospheric Sciences*, *68*(9), 1865–1881. doi: 10.1175/2011JAS3614.1

Schuddeboom, A. J., & McDonald, A. J. (2021). The Southern Ocean Radiative Bias, Cloud Compensating Errors, and Equilibrium Climate Sensitivity in CMIP6 Models. *Journal of Geophysical Research: Atmospheres*, *126*(22), 1–16. doi: 10.1029/2021JD035310

Segal, Y., & Khain, A. (2006). Dependence of droplet concentration on aerosol conditions in different cloud types: Application to droplet concentration parameterization of aerosol conditions. *Journal of Geophysical Research Atmospheres*, *111*(15). doi: 10.1029/2005JD006561

Seifert, A. (2008). A revised cloud microphysical parameterization for COSMO-LME. COSMO News Letter No. 7, Proceedings from the 8th COSMO General Meeting in Bucharest, 2006, Consortium for Small-Scale Modelling. , 25–28.

Seifert, A., & Beheng, K. D. (2006). A two-moment cloud microphysics parameterization for mixed-phase clouds. Part 1: Model description. *Meteorology and Atmospheric Physics*, *92*, 45–66. doi: 10.1007/s00703-005-0112-4

Seifert, A., Blahak, U., & Buhr, R. (2014). On the analytic approximation of bulk collision rates of non-spherical hydrometeors. *Geoscientific Model Development*, *7*(2), 463–478. doi: 10.5194/gmd-7-463-2014

Sotiropoulou, G., Vignon, E., Young, G., Morrison, H., O'Shea, S., Lachlan-Cope, T., ... Nenes, A. (2020). Secondary ice production in summer clouds over the Antarctic coast: an underappreciated process in atmospheric models. *Atmospheric Chemistry and Physics*, 1–30. doi: 10.5194/acp-2020-328

Trenberth, K. E., & Fasullo, J. T. (2010). Simulation of present-day and twenty-first-century energy budgets of the southern oceans. *Journal of Climate*, *23*(2), 440–454. doi: 10.1175/2009JCLI3152.1

Twomey, S., & Warner, J. (1967, nov). Comparison of Measurements of Cloud Droplets and Cloud Nuclei. *Journal of the Atmospheric Sciences*, *24*(6), 702–703. Retrieved from `http://journals.ametsoc.org/doi/10.1175/1520-0469(1967)024{\%}3C0702:COMOCD{\%}3E2.0.CO;2` doi: 10.1175/1520-0469(1967)024⟨0702:COMOCD⟩2.0.CO;2

Varma, V., Morgenstern, O., Field, P., Furtado, K., Williams, J., & Hyder, P. (2020). Improving the Southern Ocean cloud albedo biases in a general circulation model. *Atmospheric Chemistry and Physics*, *20*(13), 7741–7751. doi: 10.5194/acp-20-7741-2020

Vergara-Temprado, J., Miltenberger, A. K., Furtado, K., Grosvenor, D. P., Shipway, B. J., Hill, A. A., ... Carslaw, K. S. (2018). Strong control of Southern Ocean cloud reflectivity by ice-nucleating particles. *Proceedings of the National Academy of Sciences of the United States of America*, *115*(11), 2687–2692. doi: 10.1073/pnas.1721627115

Vignon, Alexander, S. P., DeMott, P. J., Sotiropoulou, G., Gerber, F., Hill, T. C., ... Berne, A. (2021). Challenging and Improving the Simulation of Mid-Level Mixed-Phase Clouds Over the High-Latitude Southern Ocean. *Journal of Geophysical Research: Atmospheres*, *126*(7), 1–21. doi: 10.1029/2020JD033490

Wood, R. (2005). Drizzle in stratiform boundary layer clouds. Part II: Microphysical aspects. *Journal of the Atmospheric Sciences*, *62*(9), 3034–3050. doi: 10.1175/JAS3530.1

Supporting Information for "An evaluation of kilometer-scale ICON simulations of mixed-phase stratocumuli over the Southern Ocean during CAPRICORN"

Veeramanikandan Ramadoss[1], Kevin Pfannkuch[1], Alain Protat[2], Yi Huang[3,4], Steven Siems[5] and Anna Possner[1]

[1]Institute for Atmospheric and Environmental Sciences, Goethe University, Frankfurt, Germany

[2]Australian Bureau of Meteorology, Melbourne, Victoria, Australia

[3]The University of Melbourne, School of Geography, Earth and Atmospheric Sciences, Melbourne, VIC, Australia

[4]Australian Research Council Centre of Excellence of Climate Extremes, Melbourne, Australia

[5]Monash University, Melbourne, VIC, Australia

Contents of this file

Corresponding author: Veeramanikandan Ramadoss, Institute for Atmospheric and Environmental Sciences, Goethe University, Altenhöferallee 1, 60438, Frankfurt/Main, Germany. (ramadoss@iau.uni-frankfurt.de)

1. PAMTRA for ICON simulations

Passive and Active Microwave TRAnsfer (PAMTRA) is made to accommodate microphysical outputs from both 1M and 2M ICON simulations (Mech et al., 2020). The active radiative transfer part includes the forward simulation of the bottom-up radar reflectivity profiles, and Doppler spectrum and its moments. The 1M scheme that simulates prognostic mass mixing ratio is assumed to have a monodisperse particle size distribution for both cloud droplet and cloud ice hydrometeors. Inverse exponential size distribution is assumed for the other hydrometeor categories. The parameters of four-parameter gamma distribution are set to transform into a monodisperse (all the four parameters = 0) and inverse exponential size distribution (shape parameter = 0 and power factor = 1) (Petty & Huang, 2011; Wu & McFarquhar, 2018; Mech et al., 2020), with the maximum fixed size for the former and size computation according to mass-size power-law relation for the latter. All six hydrometeor categories in 2M are assumed to be distributed according to modified four-parameter gamma distribution, while the sizes are computed from mass using power-law relations. In our PAMTRA offline simulations, cloud droplets, rain, graupel and hail follow mie scattering, whereas ice and snow follow self-similar Rayleigh–Gans scattering.

2. Parameterization for cloud droplet number concentration

In 2M scheme, the cloud droplet number concentration (CDNC) at the cloud base is parameterized using the regression equations with CDNC as a function of condensation nuclei (CN) concentration, width of their size distribution and cloud base velocity (Segal & Khain, 2006). The number of droplets to be added in the cloud is provided by the look-up tables for a prescribed list of number concentrations and mean radii of the CN size distribution, with the interpolated cloud base velocity and the width of CN distribution, making it prognostic in the 2M scheme.

3. Parameterization for ice crystal number concentration

In 2M scheme, the total potential ice nucleating particles (INPs) are determined based on the McCluskey, Ovadnevaite, et al. (2018) for sea spray aerosols (Equation 1) and Demott et al. (2015) for mineral dusts (Equation 2). The immersion freezing occurs in the region where the supersaturation with respect to ice is greater than 100%, the temperature is lower than -5°C, and the cloud droplet mass mixing ratio is higher than 1E-20 $\mathrm{kg\,m^{-3}}$.

$$n_{\mathrm{SSA\_INPs}}(T) = exp[-0.545(T - 273.15) + 1.0125] * S_{\mathrm{SSA}} * 0.001 \quad (1)$$

$$n_{\mathrm{dust\_INPs}}(T) = exp[0.46(273.15 - T) - 11.6] * (n_{\mathrm{500nm}})^{1.25} \quad (2)$$

Here, $n_{\mathrm{SSA\_INPs}}$ is the potential INP number concentration from the sea spray aerosols ($\mathrm{L^{-1}}$);
$n_{\mathrm{dust\_INPs}}$ is the potential INP number concentration from the mineral dust ($\mathrm{L^{-1}}$);
T is the temperature (K);
S_{SSA} is the surface area concentration of the sea spray aerosols ($\mathrm{m^2\,m^{-3}}$). The mean of S_{SSA} for the two-day period (=22.1829E-6 $\mathrm{m^2\,m^{-3}}$) is derived from McCluskey, Hill, et al. (2018);
n_{500nm} is the number concentration of mineral dust particles greater than 500 nm in size ($\mathrm{cm^{-3}}$). This value is calculated by equating the the total INP ($n_{\mathrm{SSA\_INPs}} + n_{\mathrm{dust\_INPs}}$) number concentration as 0.0046 $\mathrm{L^{-1}}$ at -20°C (McCluskey, Hill, et al., 2018) in March-April 2016.

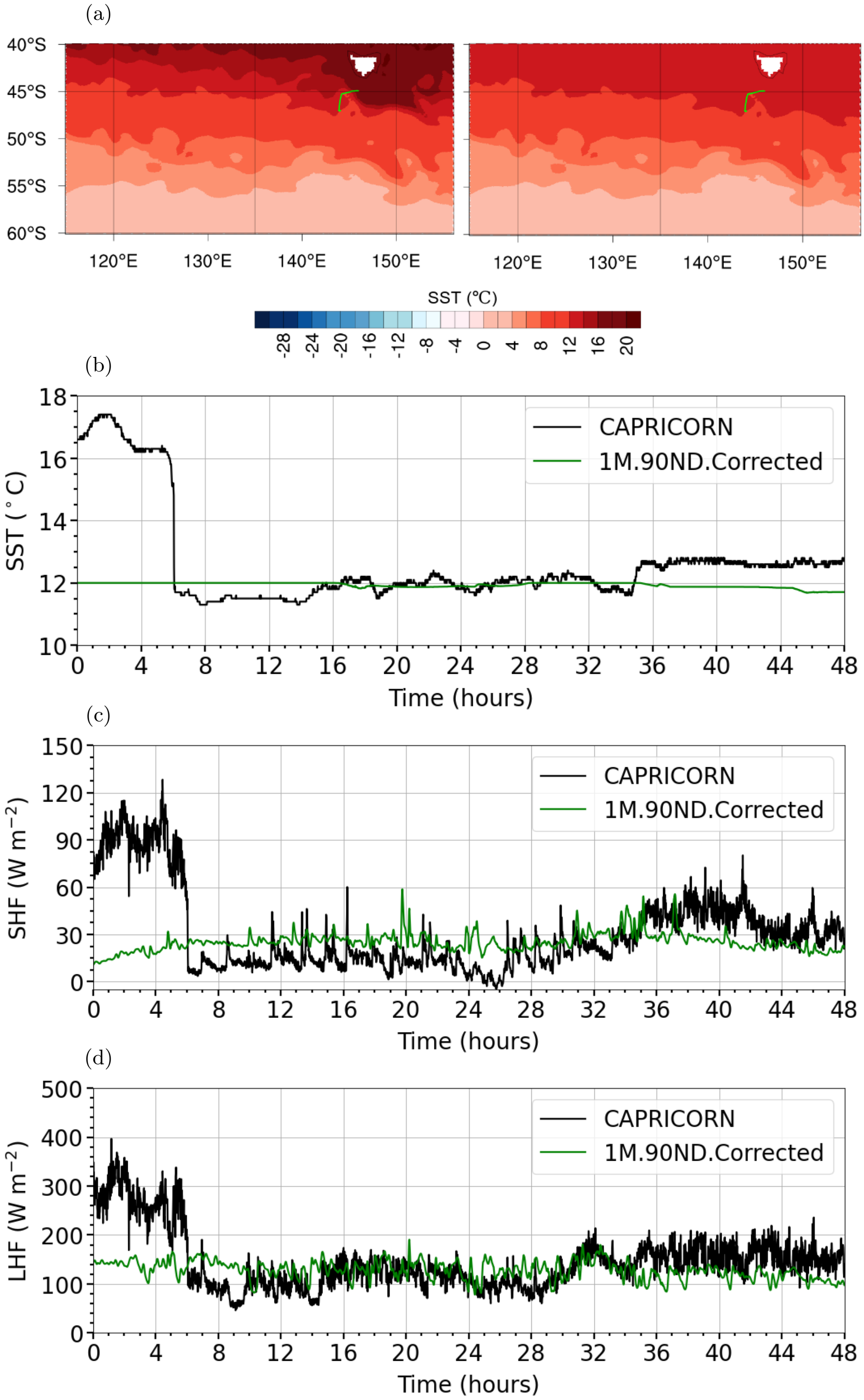

Figure S1: (a) Uncorrected (left-hand side) and corrected (right-hand side) SST contours in the simulation domain on 25$^{\text{th}}$ of March 2016 at 12:00:00 UTC with the two-day ship track (green). Time series for the entire ship track of (b) SST (°C), (c) SHF (W m^{-2}) and (d) LHF (W m^{-2}). SST, sea surface temperature; SHF, sensible heat flux; LHF, latent heat flux.

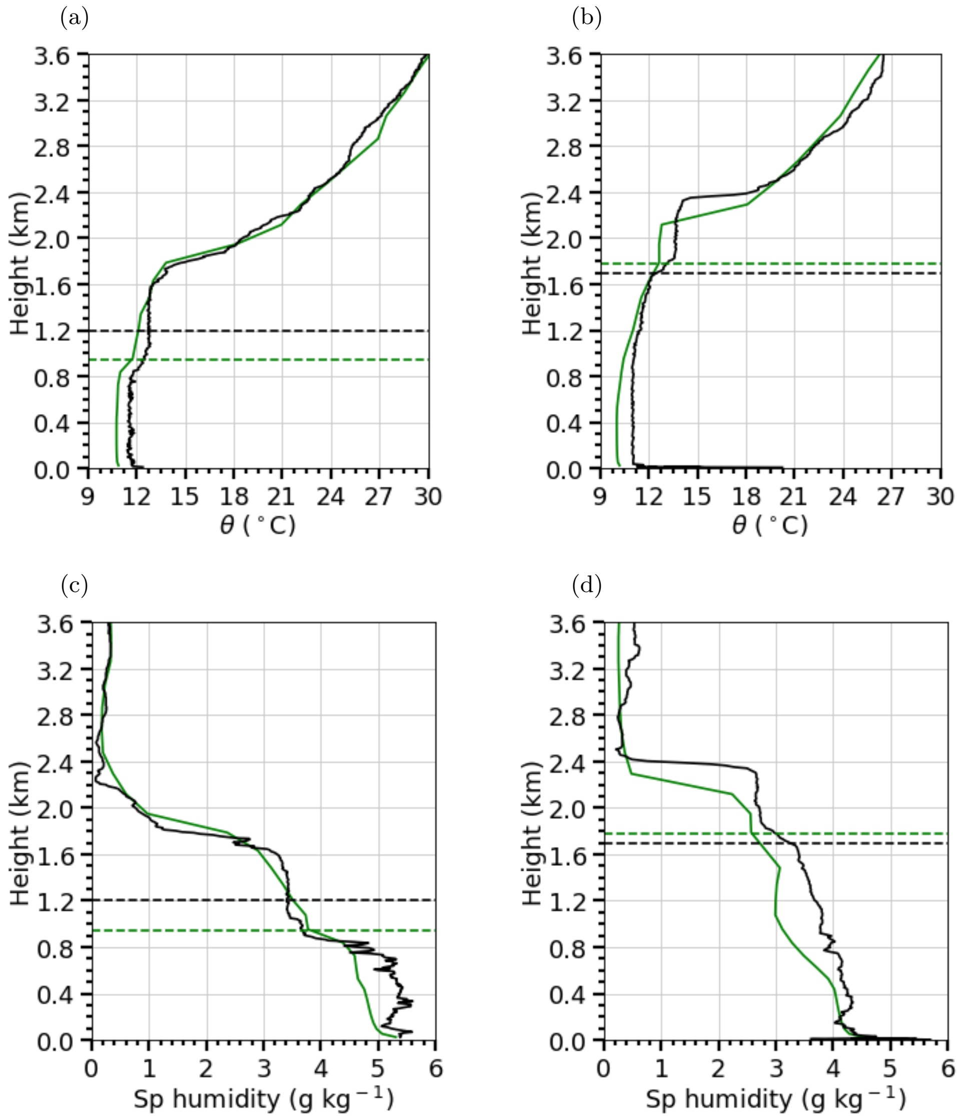

Figure S2: Thermodynamic profiles from upper-air radiosondes (black lines) and control simulation (1M.90ND - green lines) at the same location on (a),(c) 26th of March 2016 at 01:42:00 UTC and (b),(d) 26th of March 2016 at 06:24:00 UTC. Dashed lines in green (black) represent the location of simulated (observed) transition layer. θ represents potential temperature.

The boundary layer decoupling from the thermodynamic profile is identified by the presence of a transition layer that separates the cloud and subcloud layer. A strong decrease in mixing ratio and an increase in potential temperature characterize the transition layer. The conditional μ parameter which is defined as $\mu = \delta\ \theta\ /\ \delta$ P - ((0.608 θ /(1+0.608r)) δ r/ δ P) can identify the presence of transition layer when the maximum value of 'μ' is positive below the main inversion and the ratio of the maximum value of 'μ' and its average below the main inversion is greater than 1.3 (Yin & Albrecht, 2000). Note that 'θ' is the potential temperature, 'r' is the mixing ratio, and 'P' is the atmospheric pressure.

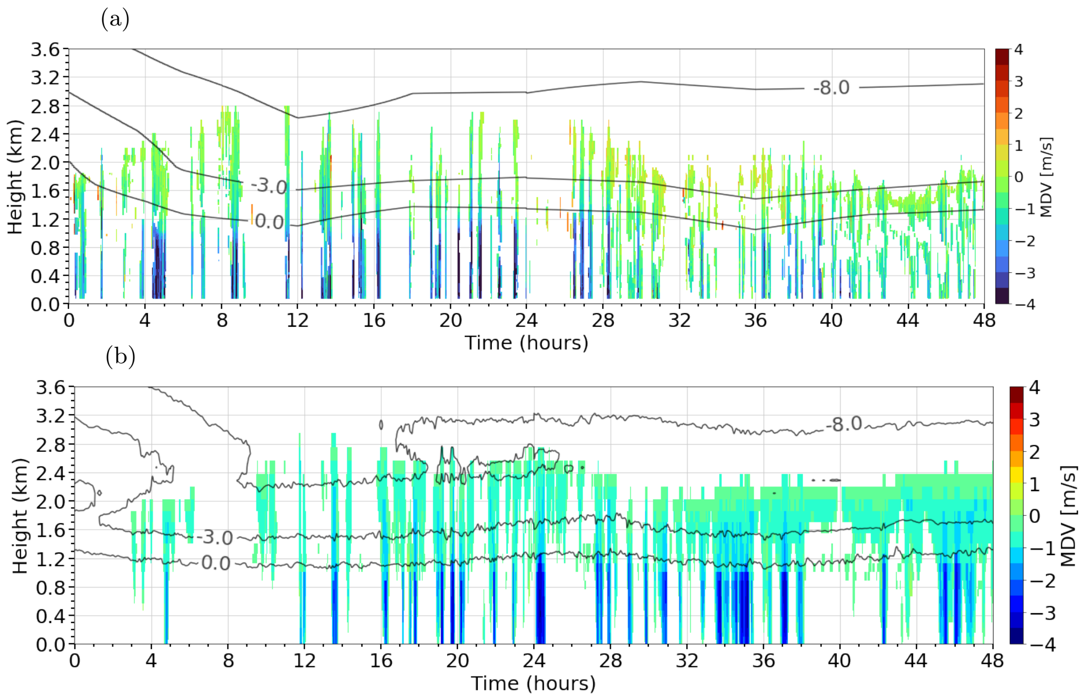

Figure S3: Time-height cross-section with 1 min temporal resolution of Mean Doppler Velocity for (a) CAPRICORN and (b) control simulation. Data is analyzed for the entire case study period (26th of March 2016 at 00:00:00 UTC to 28th of March 2016 at 00:00:00 UTC).

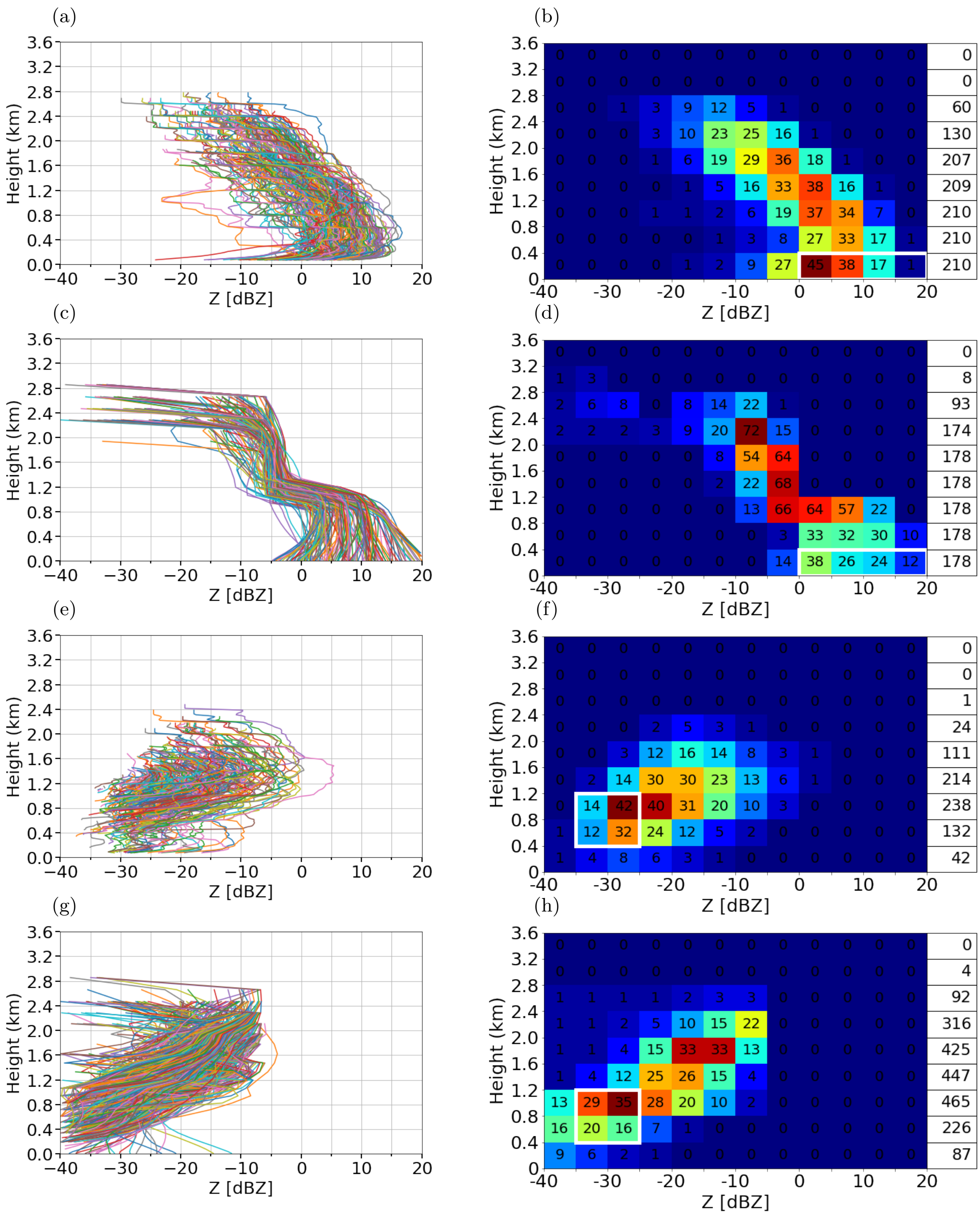

Figure S4: Along the ship track, all the continuous reflectivity streaks which are passing through the reflectivity bins enclosed by the white rectangles in (b),(d),(f),(h) are plotted with distinct coloured lines for (a),(e) CAPRICORN and (c),(g) control simulation. The number of streaks passing through each reflectivity-height bin is normalized with the total number of streaks passing through the white box (given in percentage - that shows how the streaks are distributed across the various bins) for (b),(f) CAPRICORN and (d),(h) 1M.90ND, with the total number of data for each height bin is shown on right. The reflectivity inside a certain height bin abruptly changes when the data across the reflectivity bins in that height bin exceeds 100%. Data is analyzed for the entire case study period (26th of March 2016 at 00:00:00 UTC to 28th of March 2016 at 00:00:00 UTC).

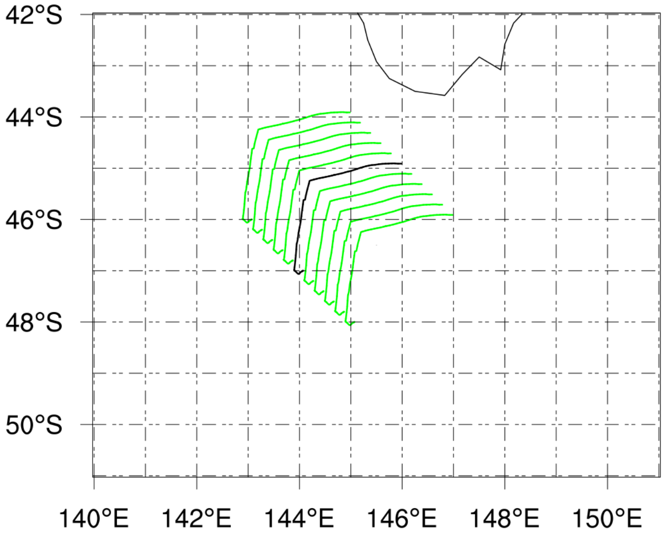

Figure S5: The two-day track (black) from CAPRICORN is offset (0.2°E, 0.2°S; 0.2°W, 0.2°N for each track) to 10 different locations (green) for quasi-ensemble analysis.

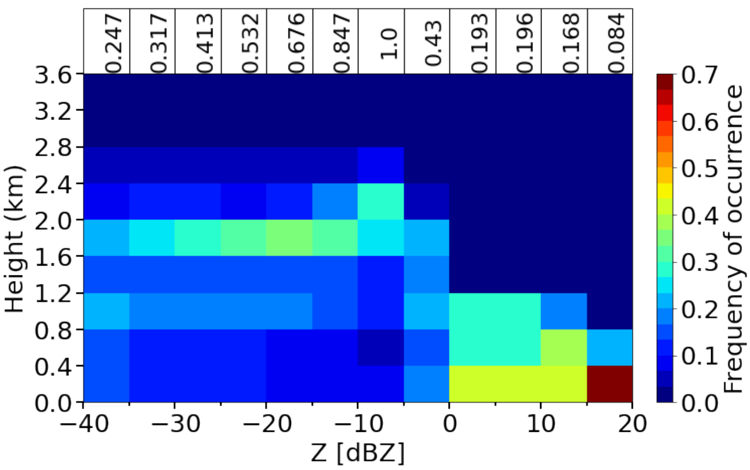

Figure S6: Normalized contoured frequency by altitude diagram with 1-min resolution for the quasi-ensemble control simulation.

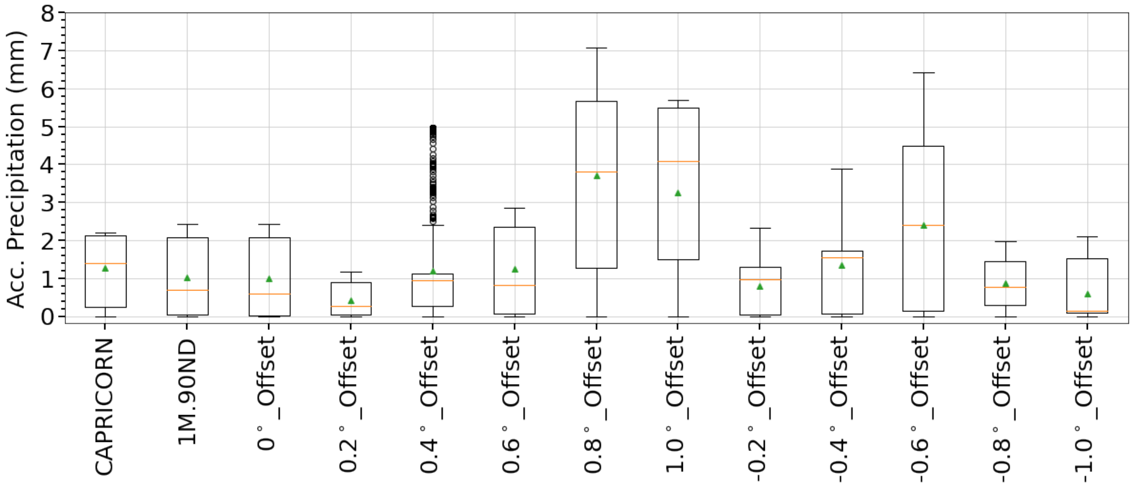

Figure S7: The spread of accumulated precipitation data for CAPRICORN, control simulation with data averaged for 2 km radius (1M.90ND) along the ship track and point data along the ship track at 10 different locations. The data from the track with no offset corresponds to 0°_Offset. The accumulated precipitation is analyzed in the tracks shifted to the south-east (0.2°_Offset, 0.4°_Offset, 0.6°_Offset, 0.8°_Offset and 1.0°_Offset) and the north-west (-0.2°_Offset, -0.4°_Offset, -0.6°_Offset, -0.8°_Offset and -1.0°_Offset) directions. Data is analyzed for the entire case study period (26^{th} of March 2016 at 00:00:00 UTC to 28^{th} of March 2016 at 00:00:00 UTC).

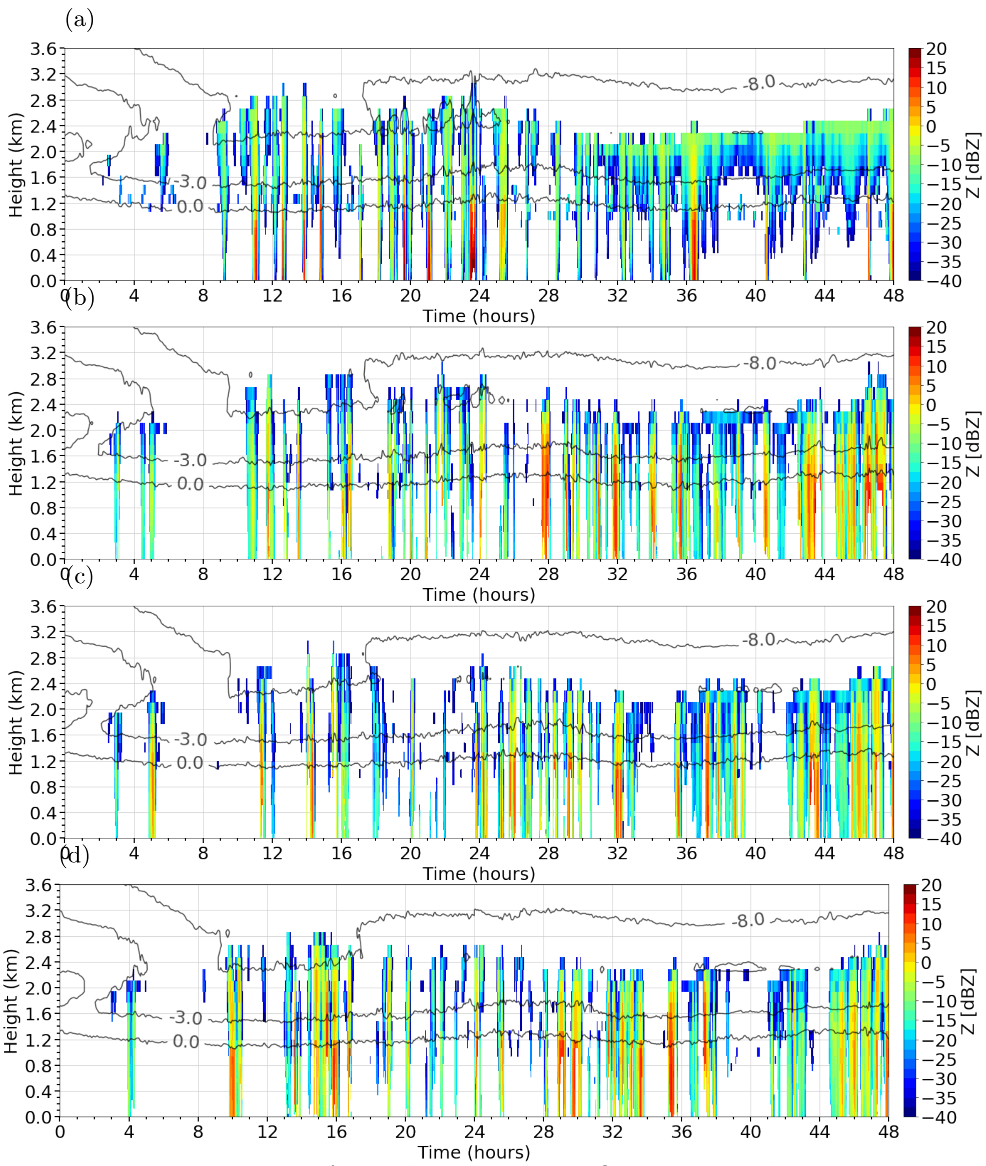

Figure S8: Time-height cross-section of simulated radar reflectivity with 1 min temporal resolution for (a) 1M.20ND, (b) 2M.P (c) 2M.HM and (d) 2M.HM.BR03. Case study period: 26th of March 2016 at 00:00:00 UTC to 28th of March 2016 at 00:00:00 UTC.

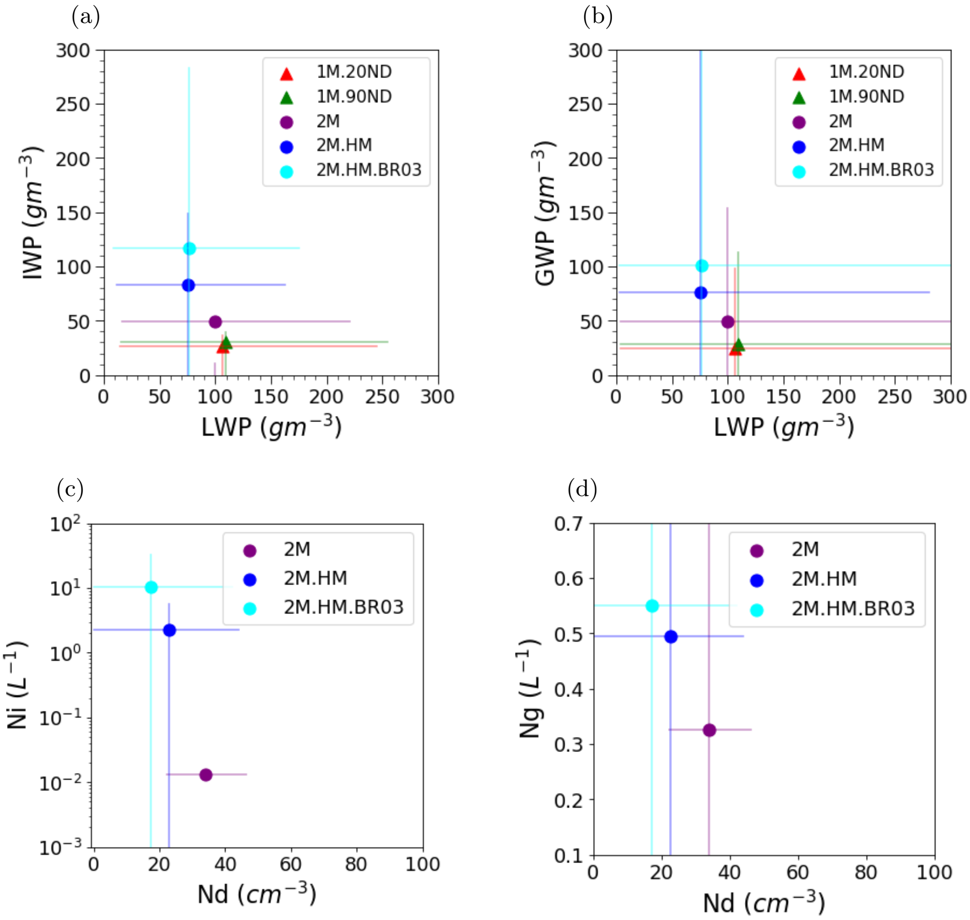

Figure S9: Spatial and temporal mean response obtained for the domain and case period of simulation in (a) IWP (all solid hydrometeors), (b) GWP, (c) ice number concentration (all solid hydrometeors), and (d) graupel number concentration. Domain is clipped around the ship track (see section 2.3).

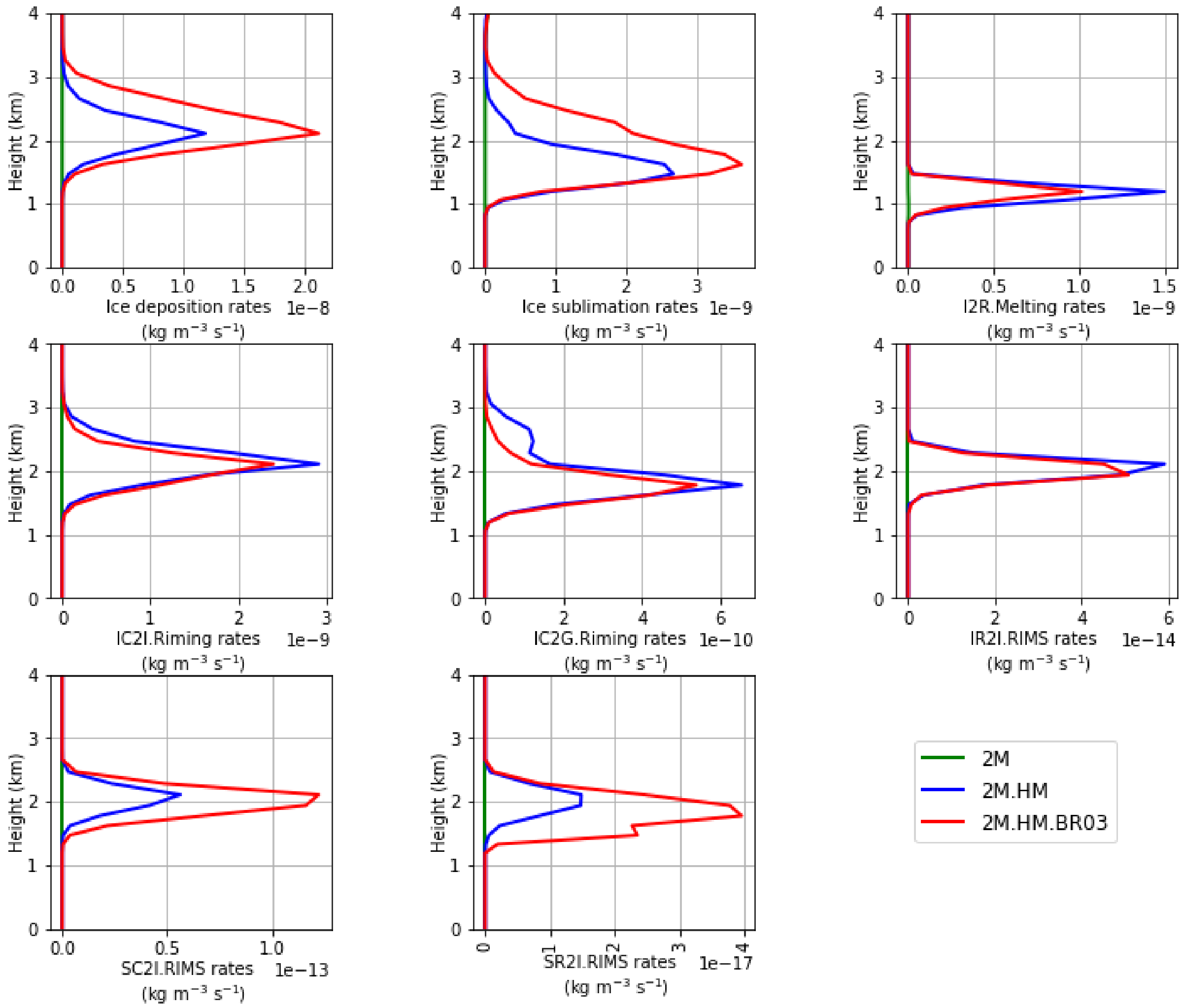

Figure S10: Spatial and temporal mean of ice microphysical processes for the entire simulation period (26$^{\text{th}}$ of March 2016 at 00:00:00 UTC to 28$^{\text{th}}$ of March 2016 at 00:00:00 UTC).

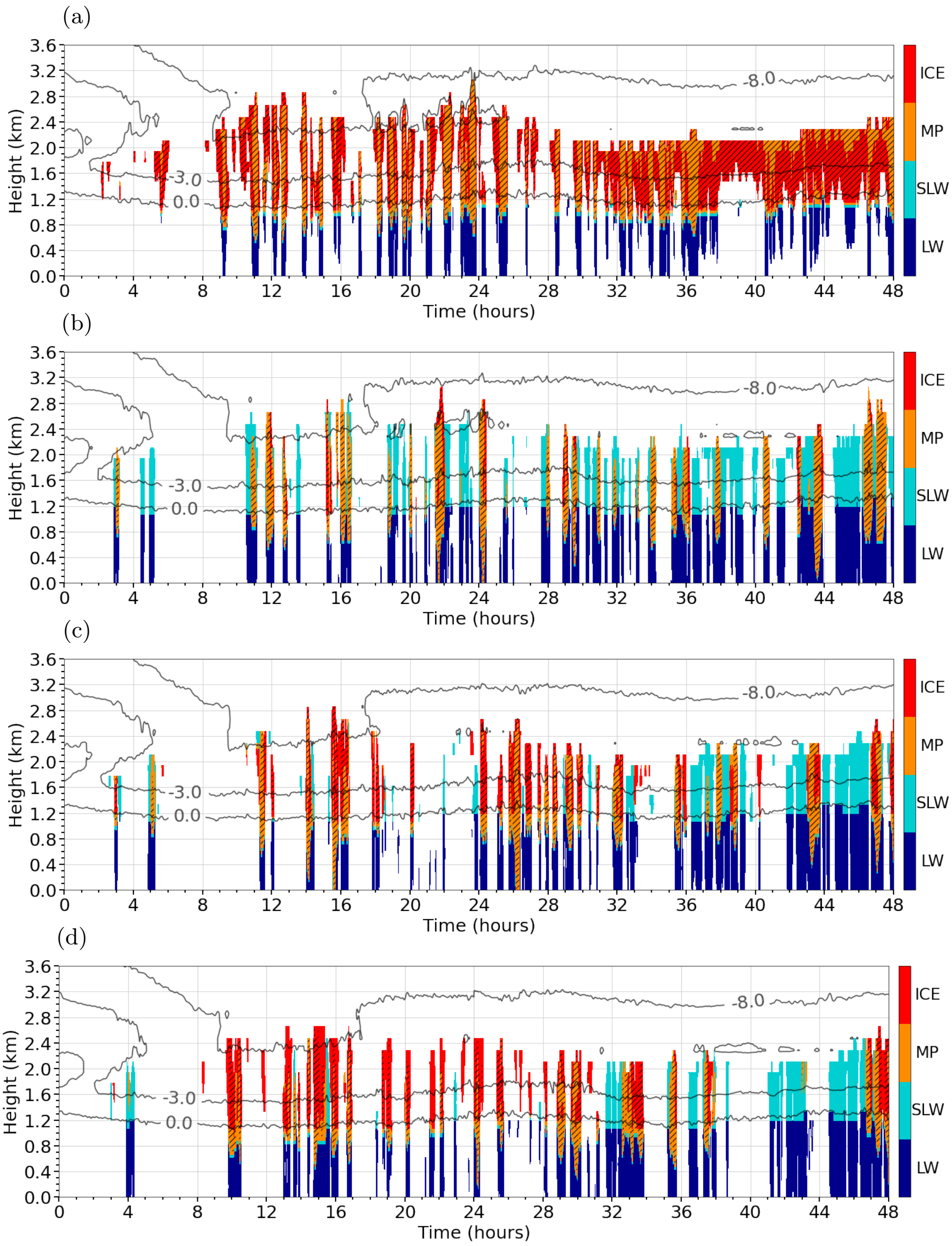

Figure S11: Time-height cross-section of simulated cloud-precipitation phase with 1 min temporal resolution for (a) 1M.20ND, (b) 2M.P (c) 2M.HM and (d) 2M.HM.BR03. Case study period: 26th of March 2016 at 00:00:00 UTC to 28th of March 2016 at 00:00:00 UTC.

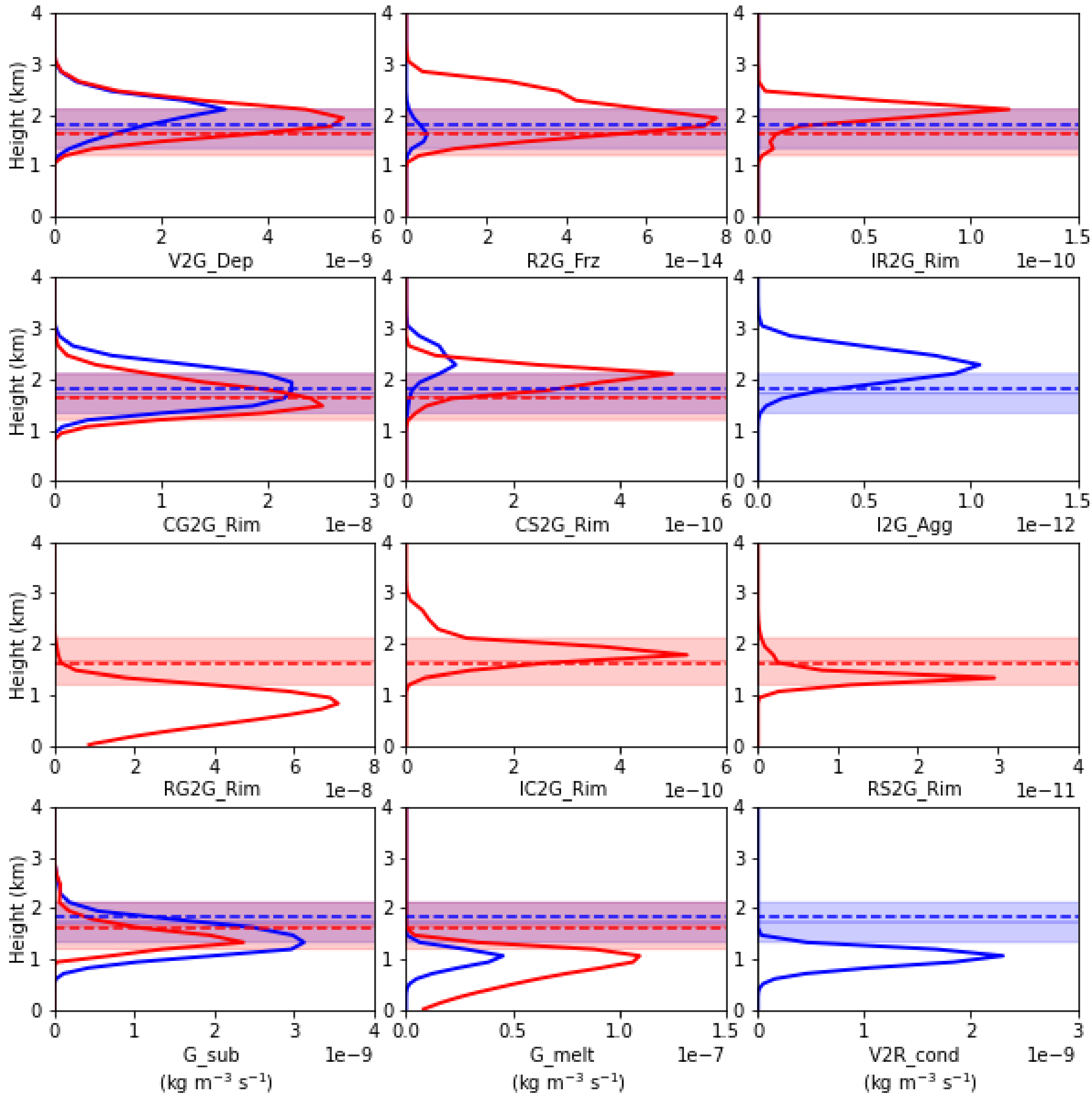

Figure S12: Spatial and temporal mean of graupel microphysical processes rates (solid lines). Dashed lines correspond to mean cloud base height. Blue and red lines represents 1M.90ND and 2M.HM simulation respectively. Shading corresponds to 20 to 80 percentile of CBH. The hourly data is processed only on 27th of March 2016.

(a)

Hydrometeor	1M.20ND (dBZ)	1M.90ND (dBZ)	2M.P (dBZ)	2M.HM (dBZ)	2M.HM.BR03 (dBZ)
All (normalized)	3.37	4.01	2.19	2.28	2.13
All	3689	3884	2174	2008	2060
Cloud water	1604	1822	579	254	367
Cloud ice	0	0	0	1296	1230
Rain	743	31	1940	921	973
Snow	3	16	0	942	1109
Graupel	3478	3665	612	756	750
Hail	-	-	10	0	0

(b)

Hydrometeor	1M.20ND (%)	1M.90ND (%)	2M.P (%)	2M.HM (%)	2M.HM.BR03 (%)
Cloud water	27.52	32.92	18.43	6.09	8.29
Cloud ice	0	0	0	31.09	27.77
Rain	12.74	0.56	61.76	22.09	21.96
Snow	0.05	0.29	0	22.59	25.03
Graupel	59.68	66.23	19.48	18.13	16.93
Hail	-	-	0.32	0	0

(c)

Hydrometeor	1M.20ND (%)	1M.90ND (%)	2M.P (%)	2M.HM (%)	2M.HM.BR03 (%)
All	-5.02	-	-44.03	-48.30	-46.96
Cloud water	-11.96	-	-68.22	-86.06	-79.86
Rain	2296.77	-	6158.06	2870.97	3038.71
Snow	-81.25	-	-100	5787.50	6831.25
Graupel	-5.10	-	-83.30	-79.37	-79.54

Table S1: Simulated bridge reflectivity analysis for the CFAD structure (-25 to 0 dBZ; 1.6 to 2 km altitude). (a) Sum of the reflectivities, (b) Percentage contribution of reflectivity of each hydrometeor with respect to the sum of individual reflectivities in every experiment and (c) Change in percentage compared to the control simulation (1M.90ND).

Experiment	Median (mm)	25^{th} percentile (mm)	75^{th} percentile (mm)
CAPRICORN	1.39	0.24	2.12
2km	0.68	0.03	2.07
0deg	0.59	0.01	2.06
0.2	0.26	0.04	0.89
0.4	0.95	0.25	1.11
0.6	0.82	0.07	2.35
0.8	3.81	1.28	5.66
1	4.10	1.50	5.50
-0.2	0.98	0.05	1.28
-0.4	1.54	0.06	1.72
-0.6	2.41	0.15	4.50
-0.8	0.76	0.29	1.44
-1	0.14	0.08	1.53

Table S2: The median, 25^{th} percentile and 75^{th} percentile of accumulated precipitation for CAPRICORN in the first row and the control simulation in all other rows. A mean value of precipitation within a 2 km radius is calculated in 1M.90ND for each coordinate along the ship track (Experiment '2km'). The point-wise precipitation data are retrieved for all other tracks (Experiment '0deg' to '-1'), with the number reflecting the degree of offset and the south-east offset being regarded a positive direction and the north-west offset being considered a negative direction.

Hydrometeor	Below_freezing_line		Above_freezing_line	
	min	max	min	max
All	-40	20	-40	0.2
Cloud water	-40	-6.6	-40	-6
Ice	-	-	-40	-25.4
Rain	-40	20	-40	-1.6
Snow	-	-	-40	-13.7
Graupel	-40	4	-40	3.8

Table S3: The reflectivity range (dBZ) for each hydrometeors for control simulation. The row 'All' represents when all the hydrometeors are active in reflectivity calculation. The tentative freezing line has been set at 1.2 km.

References

Demott, P. J., Prenni, A. J., McMeeking, G. R., Sullivan, R. C., Petters, M. D., Tobo, Y., … Kreidenweis, S. M. (2015). Integrating laboratory and field data to quantify the immersion freezing ice nucleation activity of mineral dust particles. *Atmospheric Chemistry and Physics*, *15*(1), 393–409. doi: 10.5194/acp-15-393-2015

McCluskey, C. S., Hill, T. C., Humphries, R. S., Rauker, A. M., Moreau, S., Strutton, P. G., … DeMott, P. J. (2018). Observations of Ice Nucleating Particles Over Southern Ocean Waters. *Geophysical Research Letters*, *45*(21), 11,989–11,997. doi: 10.1029/2018GL079981

McCluskey, C. S., Ovadnevaite, J., Rinaldi, M., Atkinson, J., Belosi, F., Ceburnis, D., … DeMott, P. J. (2018). Marine and Terrestrial Organic Ice-Nucleating Particles in Pristine Marine to Continentally Influenced Northeast Atlantic Air Masses. *Journal of Geophysical Research: Atmospheres*, *123*(11), 6196–6212. doi: 10.1029/2017JD028033

Mech, M., Maahn, M., Kneifel, S., Ori, D., Orlandi, E., Kollias, P., … Crewell, S. (2020). PAMTRA 1.0: The Passive and Active Microwave radiative TRAnsfer tool for simulating radiometer and radar measurements of the cloudy atmosphere. *Geoscientific Model Development*, *13*(9), 4229–4251. doi: 10.5194/gmd-13-4229-2020

Petty, G. W., & Huang, W. (2011). The modified gamma size distribution applied to inhomogeneous and nonspherical particles: Key relationships and conversions. *Journal of the Atmospheric Sciences*, *68*(7), 1460–1473. doi: 10.1175/2011JAS3645.1

Segal, Y., & Khain, A. (2006). Dependence of droplet concentration on aerosol conditions in different cloud types: Application to droplet concentration parameterization of aerosol conditions. *Journal of Geophysical Research Atmospheres*, *111*(15). doi: 10.1029/2005JD006561

Wu, W., & McFarquhar, G. M. (2018). Statistical theory on the functional form of cloud particle size distributions. *Journal of the Atmospheric Sciences*, *75*(8), 2801–2814. doi: 10.1175/JAS-D-17-0164.1

Yin, B., & Albrecht, B. A. (2000, may). Spatial Variability of Atmospheric Boundary Layer Structure over the Eastern Equatorial Pacific. *Journal of Climate*, *13*(9), 1574–1592. Retrieved from `http://journals.ametsoc.org/doi/10.1175/1520-0442(2000)013{\%}3C1574:SVOABL{\%}3E2.0.CO;2` doi: 10.1175/1520-0442(2000)013⟨1574:SVOABL⟩2.0.CO;2